

A multiwavelength light curve analysis of the classical nova KT Eri: Optical contribution from a large irradiated accretion disk

IZUMI HACHISU ¹, MARIKO KATO ² AND FREDERICK M. WALTER ³

¹*Department of Earth Science and Astronomy, College of Arts and Sciences, University of Tokyo, Komaba 3-8-1, Meguro-ku, Tokyo 153-8902, Japan*

²*Department of Astronomy, Keio University, Hiyoshi 4-1-1, Kouhoku-ku, Yokohama 223-8521, Japan*

³*Department of Physics and Astronomy, Stony Brook University, Stony Brook, New York, NY 11794, USA*

ABSTRACT

KT Eri is a classical nova which went into outburst in 2009. Recent photometric analysis in quiescence indicates a relatively longer orbital period of 2.6 days, so that KT Eri could host a very bright accretion disk during the outburst like in the recurrent nova U Sco, the orbital period of which is 1.23 days. We reproduced the optical V light curve as well as the supersoft X-ray light curve of KT Eri in outburst, assuming a large irradiated disk during a nova wind phase of the outburst while a normal size disk after the nova winds stop. This result is consistent with the temporal variation of wide-band V brightness that varies almost with the intermediate-band Strömgen y brightness, because the V flux is dominated by continuum radiation, the origin of which is a photospheric emission from the very bright disk. We obtained the white dwarf mass to be $M_{\text{WD}} = 1.3 \pm 0.02 M_{\odot}$, the hydrogen-burning turnoff epoch to be ~ 240 days after the outburst, the distance modulus in the V band to be $(m - M)_V = 13.4 \pm 0.2$, and the distance to KT Eri to be $d = 4.2 \pm 0.4$ kpc for the reddening of $E(B - V) = 0.08$. The peak absolute V brightness is about $M_{V,\text{max}} = -8.0$ and the corresponding recurrence time is $\sim 3,000$ yr from its ignition mass together with the mean mass-accretion rate of $\dot{M}_{\text{acc}} \sim 1 \times 10^{-9} M_{\odot} \text{ yr}^{-1}$ in quiescence. Thus, we suggest that KT Eri is not a recurrent nova.

Keywords: binaries: close — novae, cataclysmic variables — stars: individual (KT Eri) — stars: winds — X-rays: stars

1. INTRODUCTION

KT Eri is a classical nova, discovered on UT 2009 November 25 (JD 2,455,160.5) at $V = 8.1$ by K. Itagaki (Yamaoka et al. 2009). Based on the data of Solar Mass Ejection Imager (SMEI), Hounsell et al. (2010) constructed a pre-discovery light curve (Figure 1a). The SMEI quantum efficiency has a peak at $\lambda \sim 700$ nm with an FWHM of $\Delta\lambda = 300$ nm. KT Eri had already brightened up to 8.4 mag on UT 2009 November 13.67 (JD 2,455,149.17) and then reached maximum at 5.4 mag on UT 2009 November 14.67 (JD 2,455,150.17). The pre-discovery CCD magnitudes were also reported by Ootsuki et al. (2009). Hounsell et al. (2010) estimated the decay times from the peak by 2 and 3 mag to

be $t_2 = 6.6$ days and $t_3 = 13.6$ days, respectively. Thus, KT Eri belongs to the class of very fast novae.¹

Many photometric data were obtained after the discovery (e.g., Hung et al. 2012). We plot the V data (filled green squares) in Figure 1a, taken from the archives of the Variable Star Observers League of Japan (VSOLJ), American Association of Variable Star Observers (AAVSO), SMARTS (Walter et al. 2012), those reported in IAU Circular No.9098 (Ootsuki et al. 2009), and Imamura & Tanabe (2012). Imamura & Tanabe (2012) reported their $BVyR_C$ photometry. We also plot their y magnitude data (filled black triangles) in Figure 1a.

¹ The nova speed class is defined by t_2 or t_3 , for example, very fast novae ($t_2 \leq 10$ days), fast novae ($10 < t_2 \leq 25$ days), moderately fast novae ($25 < t_2 \leq 80$ days), slow novae ($80 < t_2 \leq 150$ days), and very slow novae ($150 < t_2 \leq 250$ days), as defined by Payne-Gaposchkin (1957).

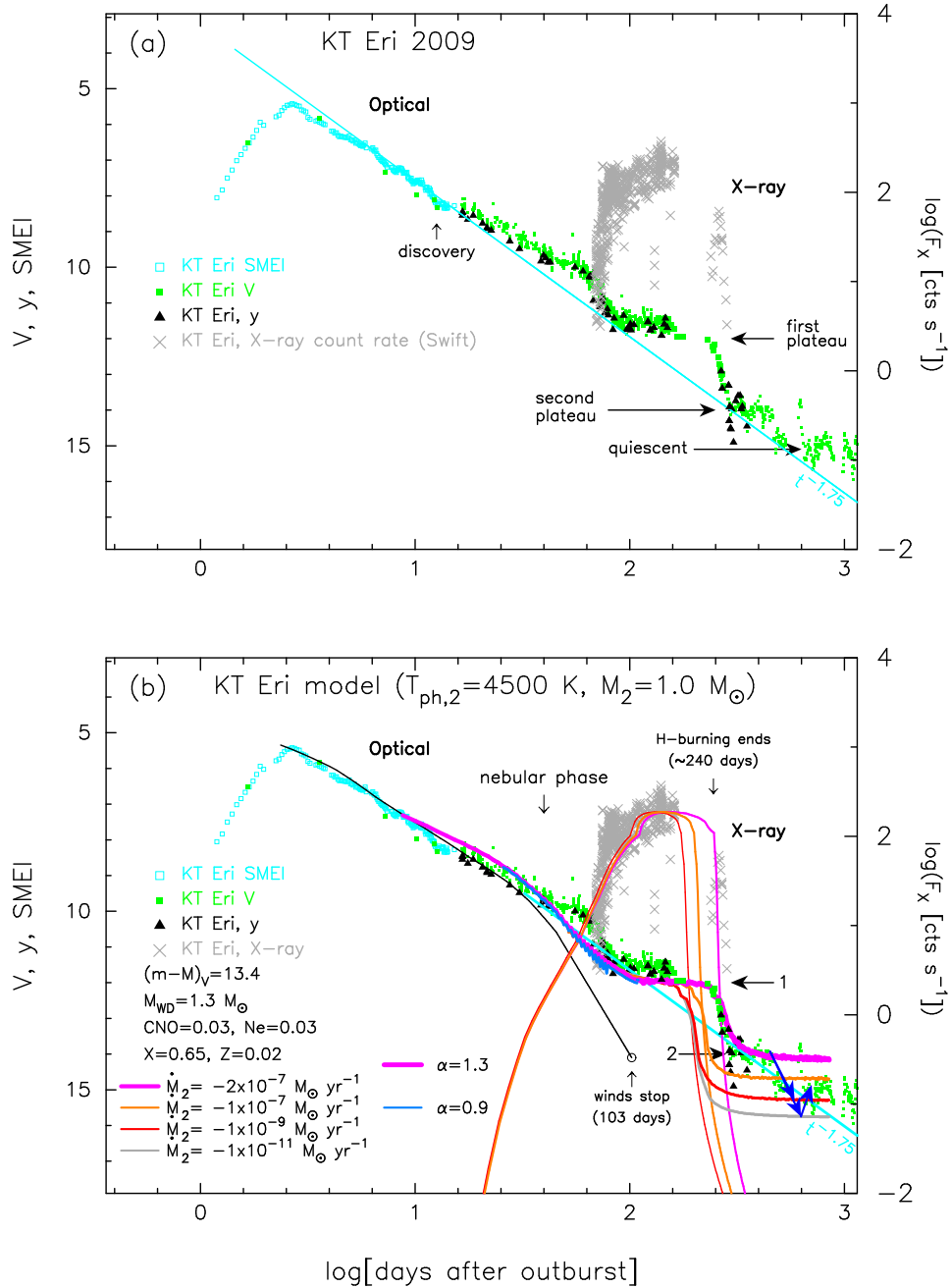


Figure 1. (a) The V , y , and SMEI magnitudes of KT Eri against a logarithmic time. We assume the outburst day of $t_{\text{OB}} = \text{JD } 2,455,147.5$, 2.7 days before optical (SMEI) maximum. The V data are taken from VSOLJ, AAVSO, SMARTS (Walter et al. 2012), and IAU Circular No.9098 (Ootsuki et al. 2009). The y data from Imamura & Tanabe (2012). The SMEI data from Hounsell et al. (2010). The Swift X-ray (0.3–10.0 keV) count rates are also added, taken from the Swift website (Evans et al. 2009). The global decay trend is described by the universal decline law of $L_V \propto t^{-1.75}$ (straight cyan line labeled $t^{-1.75}$; Hachisu & Kato 2006, 2023). (b) Same as panel (a), but we overplot our model light curves (see Appendices A and B for details). We assume a Roche-lobe-filling companion star with the photospheric temperature of $T_{\text{ph},2} = 4,500 \text{ K}$ and mass of $M_2 = 1.0 M_\odot$. The black line is our free-free (FF) + photospheric blackbody (BB) model light curve of a $1.3 M_\odot$ white dwarf (WD). The thick magenta, orange, red, and gray lines denote the model V light curves for the $1.3 M_\odot$ WD with different mass-accretion rates (see Table 1 and Appendix B) assuming a large disk size of $\alpha = 1.3$ (magenta line) during the nova wind phase. We added another case of $\alpha = 0.9$ (cyan-blue line) for comparison. The thin colored lines are for the corresponding model X-ray fluxes (0.3–10.0 keV). The blue lines with an arrow depict temporal variations of the brightness against temporal changes of mass-accretion rate in quiescence.

Optical spectroscopy of KT Eri were reported by Ragan et al. (2009), Bode et al. (2009), Imamura & Tanabe (2012), Arai et al. (2013), Ribeiro et al. (2013), and Munari et al. (2014). The broad Balmer emission showed $\text{FWHM} \sim 3200\text{--}3400 \text{ km s}^{-1}$ (Maehara et al. 2009; Maehara & Imamura 2009) or the He I $1.083\mu\text{m}$ line had $\text{FWHM} \sim 4000 \text{ km s}^{-1}$ and its P-Cygni absorption profile was extending to 3600 km s^{-1} on UT 2009 November 26.5 (JD 2,455,162; Rudy et al. 2009). Ribeiro et al. (2013) analyzed the H α line profiles between 42 and 73 days after optical maximum and proposed a model of dumbbell shaped expanding ejecta with the expanding velocity of $v_{\text{exp}} = 2800 \pm 200 \text{ km s}^{-1}$ and inclination angle of 58_{-7}^{+6} deg.

X-rays were observed with Swift (Bode et al. 2009; Beardmore et al. 2010; Schwarz et al. 2011), Chandra (Ness et al. 2011; Sun et al. 2020; Pei et al. 2021), and XMM-Newton (Sun et al. 2020). The bright supersoft X-ray source (SSS) phase started ~ 65 days and ended ~ 280 days after optical maximum (Figure 1a). KT Eri was also observed with radio (O’Brien et al. 2010) and near infra-red (Rudy et al. 2009; Raj et al. 2013).

Jurdana-Šepić et al. (2012) searched the archival plates of the Harvard College Observatory for a previous outburst of KT Eri. They found no outbursts between 1888 and 1962, and concluded that, if KT Eri is a recurrent nova, it should have a recurrence time of centuries. Darnley et al. (2012) discussed the positions of KT Eri in various color-magnitude diagrams and concluded that the companion star of KT Eri is a red giant, less evolved than that of RS Oph and T CrB.

Schaefer et al. (2022) pointed out two distinct plateau phases in the BVI_C light curves: the first one is coincident with the supersoft X-ray source (SSS) phase (Figure 1a). They obtained the orbital period to be $P_{\text{orb}} = 2.6$ days both from the ~ 0.2 mag TESS photometric variation and the orbital velocity variation. This P_{orb} is exceptionally long for classical novae. Thus, KT Eri resembles recurrent novae both in the optical plateau during the SSS phase and in the long orbital period. Schaefer et al. (2022) also pointed out a large temporal variation of the V light curve in quiescence, as large as $\Delta V \sim 1.5$, and raised the question on the origin of such a large variation, the timescale of which is from 1 month to 3 months.

Schaefer et al. (2022) estimated the mass-accretion rate on to the white dwarf (WD) to be $\sim 3.5 \times 10^{-7} (d/5.1 \text{ kpc})^2 M_{\odot} \text{ yr}^{-1}$ from the brightness of a viscous disk and companion star, and concluded that KT Eri is a recurrent nova with recurrence time of

40–50 yr. Here, d is the distance to KT Eri. From the theoretical point of view, however, a nova outburst never occurs for such a high mass-accretion rate of $\sim 3.5 \times 10^{-7} M_{\odot} \text{ yr}^{-1}$ (e.g., Wolf et al. 2013; Kato et al. 2014, for recent estimates). Sun et al. (2020) reported a much smaller mass-accretion rate of $\dot{M}_{\text{acc}} \approx 1.9 \times 10^{-10} (d/3.7 \text{ kpc})^2 M_{\odot} \text{ yr}^{-1}$ based on their XMM Newton X-ray observation on UT 2018 February 15, about 8.3 yr after the outburst.

In the present paper, we propose a sophisticated model for the KT Eri 2009 outburst that explains the puzzling observational properties mentioned above. Our model consists of a WD, accretion disk, and companion star. We include the irradiation effects of the disk and companion star, while Schaefer et al. (2022) did not take into account the irradiation effects in their analysis.

Our paper is organized as follows. First we present a summary of optical and X-ray observations with our quick interpretation in Section 2. Discussion and conclusions follow in Sections 3 and 4, respectively. Next, in Appendix A, we describe our free-free emission model light curves for the V and y bands and reproduce an early phase of the V, y light curves and later supersoft X-ray light curve. Appendix B is devoted to calculation of the model V, y light curves based on our irradiated disk model, to reproduce the V, y light curves of KT Eri in the SSS and later phases. To estimate the distance to the nova, the time-stretching method is applied to KT Eri in Appendix C.

2. OBSERVATIONAL SUMMARY AND QUICK INTERPRETATION

Figure 1a shows the optical and X-ray light curves for the KT Eri 2009 outburst in a logarithmic time. The origin of the time is the outburst day. Here, we adopt the outburst day of $t_{\text{OB}} = \text{JD } 2,455,147.5$ (UT 2009 November 12.0), i.e., 2.7 days before the SMEI maximum (Hounsell et al. 2010).

We estimated the outburst day from the rising trend in the SMEI light curve by extending the rising trend down to the quiescent brightness of $V \sim 15$ mag. If an X-ray flash of KT Eri was observed like in the classical nova YZ Ret (König et al. 2022), we are able to constrain the outburst day much more accurately (e.g., Kato et al. 2022b,c). This $t_{\text{peak}} = 2.7$ days, the days from the outburst to optical maximum, is broadly consistent with $t_{\text{peak}} = 2.5$ days for a self-consistent nova model of a $1.3 M_{\odot}$ WD with the mass-accretion rate of $\dot{M}_{\text{acc}} = 2 \times 10^{-9} M_{\odot} \text{ yr}^{-1}$ (model M13C10; Kato et al. 2024).

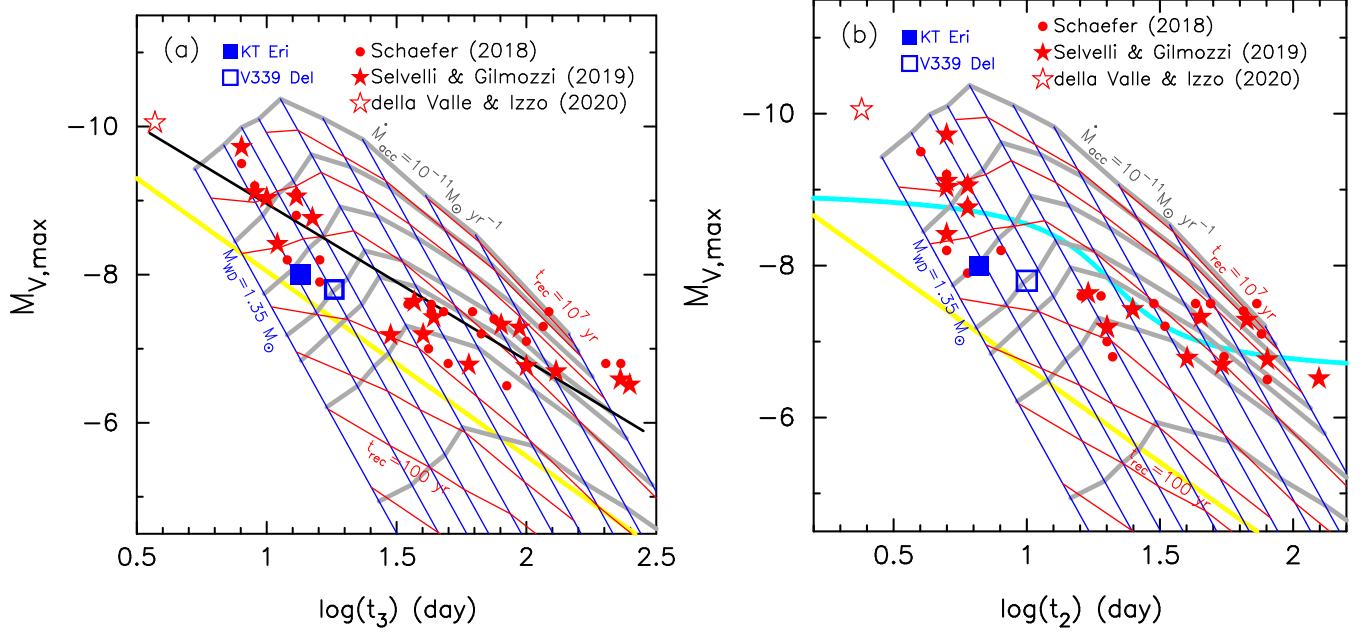


Figure 2. The maximum absolute V magnitude against the rate of decline (MMRD) diagrams for selected novae; (a) t_3 - $M_{V,\max}$ and (b) t_2 - $M_{V,\max}$. The filled blue square represents the position of KT Eri. The open blue square is V339 Del, taken from Hachisu et al. (2024). We add the MMRD points of some selected galactic novae. The filled red circles represent novae taken from “Golden sample” of Schaefer (2018), from which we exclude recurrent novae and V1330 Cyg. The filled stars are novae taken from Selvelli & Gilmozzi (2019). The open star is V1500 Cyg taken from della Valle & Izzo (2020). The blue lines indicate model equi-WD mass lines, from left to right, 1.35, 1.3, 1.25, 1.2, 1.1, 1.0, 0.9, 0.8, 0.7, and $0.6 M_{\odot}$; the thick solid gray lines denote model equi-mass accretion rate (\dot{M}_{acc}) lines, from lower to upper, 3×10^{-8} , 1×10^{-8} , 5×10^{-9} , 3×10^{-9} , 1×10^{-9} , 1×10^{-10} , and $1 \times 10^{-11} M_{\odot} \text{ yr}^{-1}$; the red lines represent model equi-recurrence time lines, from lower to upper, $t_{\text{rec}} = 30, 100, 300, 1000, 10000, 10^5, 10^6,$ and 10^7 yr. These lines are taken from Hachisu et al. (2020) based on the universal decline law of novae and model calculation of mass accretion onto each WD. The thick yellow line corresponds to the $x_0 = 2$ line (Hachisu et al. 2020), below which the models are not valid. Two empirical MMRD relations are added by the thick solid black line (Selvelli & Gilmozzi 2019) in panel (a) and by the thick solid cyan line (della Valle & Izzo 2020) in panel (b). Many recurrent novae are located in the lower-left portion of panels (a) and (b) (see, e.g., Shafter et al. 2023), and are below the solid yellow lines. Therefore, Hachisu et al. (2024)’s model lines could not be applied to recurrent novae.

The characteristic properties of the light curves of KT Eri as follows:

- (1) The SMEI magnitude reaches maximum 2.7 days after the outburst and then declines almost along the universal decline law of $L_{\text{SMEI}} \propto t^{-1.75}$ with $t_2 = 6.6$ days and $t_3 = 13.6$ days (Hounsell et al. 2010).
- (2) The optical V and Strömgren y magnitudes of KT Eri declined almost in the same way and did not depart from each other (Imamura & Tanabe 2012).
- (3) The V, y light curves show two distinct plateau phases, the first is at $V \sim 12.0$ between days 80 and 240 after maximum and the second is at $V \sim 14.1$ from 300 to 440 days after maximum (Schaefer et al. 2022).
- (4) The first plateau appears almost during the same period as the SSS phase. However, a close look

at the timing indicates that it starts slightly later than the rise of soft X-ray count rate and ends slightly before the decay of X-ray.

- (5) After the second plateau, the V brightness drops to $V \sim 15.1$, accompanying a large amplitude variation of $\Delta V \sim 1.5$ –2 and timescales of up and down from 1 month to 3 months (Schaefer et al. 2022).

In what follows, we explain how these properties make KT Eri an outlier of classical novae and give a quick understanding of our binary model.

2.1. Distance and reddening

The distance and reddening are critically important to estimate the absolute brightness of the nova. The distance was estimated to be $d = 4.1_{-0.4}^{+0.5}$ kpc by Bailer-Jones et al. (2021) based on the Gaia eDR3 parallax. The extinction $E(B - V) = 0.08$ was given by Ragan et al. (2009) from the Na I D1 line width and the

relation of [Munari & Zwitter \(1997\)](#). Then, we have the distance modulus in the V band of $(m-M)_V = 13.3 \pm 0.3$ from

$$(m-M)_V = 5 \log(d/10 \text{ pc}) + 3.1E(B-V), \quad (1)$$

where d is the distance and the coefficient of $R_V = 3.1$ is taken from [Rieke & Lebofsky \(1985\)](#).

Assuming a different prior from that of the Gaia team in a Bayesian calculation, [Schaefer et al. \(2022\)](#) obtained $d = 5110_{-430}^{+920}$ pc based on the same eDR3 parallax. This gives a larger distance modulus in the V band of $(m-M)_V = 13.8_{-0.2}^{+0.4}$. It is however noted that [Schaefer \(2022b\)](#) adopted $d = 4211_{-296}^{+466}$ pc for KT Eri. If we adopt this distance, we have $(m-M)_V = 13.4 \pm 0.2$.

We also estimate the distance modulus to KT Eri by comparing the intrinsic brightnesses of well studied novae, LV Vul and V339 Del, whose distance moduli are well determined by [Hachisu et al. \(2024\)](#). We obtained a similar distance modulus in the V band to KT Eri to be $(m-M)_V = 13.4 \pm 0.2$ (see Appendix C).

Figure 1b shows our $1.3 M_\odot$ WD model that is chosen to fit with the early light curve, adopting $(m-M)_V = 13.4$ (see Section A for details). If we adopt $(m-M)_V = 13.8$, our model V light curve (black line) will be parallel but 0.4 mag below the observation. Thus, we adopted $d = 4.2 \pm 0.4$ kpc, $E(B-V) = 0.08$, and $(m-M)_V = 13.4 \pm 0.2$.

2.2. Peak magnitude: WD mass, mass-accretion rate, and recurrence time

Adopting $(m-M)_V = 13.4$, the absolute peak V brightness of KT Eri is calculated from $M_{V,\max} = m_{V,\max} - (m-M)_V = 5.4 - 13.4 = -8.0$. [Hounsell et al. \(2010\)](#) obtained the decay times of $t_2 = 6.6$ and $t_3 = 13.6$ days. We plot these values in the maximum magnitude versus rate of decline (MMRD) diagram with other classical novae in Figure 2. KT Eri (filled blue square) is located close to the classical nova V339 Del (open blue square) and among the other well observed classical novae. Note that the distribution of novae in these MMRD plots is affected by the observational selection effect, especially in the lower-left portion of each plots (e.g., [Shafter et al. 2023](#)), because faint and fast decay novae are easily missed.

[Hachisu et al. \(2020\)](#) obtained theoretical peak absolute V magnitudes $M_{V,\max}$ and corresponding theoretical $t_3 - M_{V,\max}$ and $t_2 - M_{V,\max}$ based on a number of theoretical light curves for different mass-accretion rates \dot{M}_{acc} and WD masses M_{WD} . Figure 2 also shows theoretical lines that connect a specific WD mass, recurrence period, or mass accretion rate, from their theoretical database ([Hachisu et al. 2020](#)).

If we fix the WD mass, a nova becomes brighter (smaller $M_{V,\max}$) and faster (smaller t_3 and t_2) for a smaller mass-accretion rate (and a longer recurrence time). The position of KT Eri (filled blue square) is located close to the blue line of $M_{\text{WD}} = 1.3 M_\odot$ and the gray line of $\dot{M}_{\text{acc}} = 1 \times 10^{-9} M_\odot \text{ yr}^{-1}$. The recurrence time is estimated from two red lines of $\tau_{\text{rec}} = 1000$ yr and $\tau_{\text{rec}} = 10,000$ yr to be about $\tau_{\text{rec}} \sim 3,000$ yr. Both the diagrams of Figure 2a ($t_3 - M_{V,\max}$) and Figure 2b ($t_2 - M_{V,\max}$) give a similar result. It should be again noted that the $t_{\text{peak}} = 2.7$ days (from the outburst to optical maximum) is roughly consistent with a self-consistent nova model of a $1.3 M_\odot$ WD with the mass-accretion rate of $\dot{M}_{\text{acc}} = 2 \times 10^{-9} M_\odot \text{ yr}^{-1}$ (model M13C10; $t_{\text{peak}} = 2.5$ days; [Kato et al. 2024](#)). Thus, it is unlikely that KT Eri is a recurrent nova with recurrence time of 40–50 yr ([Schaefer et al. 2022](#)). This will be discussed in Section 3.1.

2.3. V, y light curves in the early phase: WD mass

A nova starts from unstable hydrogen burning on a WD. Then, a hydrogen-rich envelope of the WD expands and emits strong winds (e.g., [Kato et al. 2022a](#), for a recent nova calculation). Free-free emission from the nova winds dominates the optical flux of a nova (e.g., [Gallagher & Ney 1976](#); [Ennis et al. 1977](#)). [Hachisu & Kato \(2006\)](#) modeled nova light curves for the free-free emission based on the optically thick winds calculated by [Kato & Hachisu \(1994\)](#), the V flux of which can be simplified as

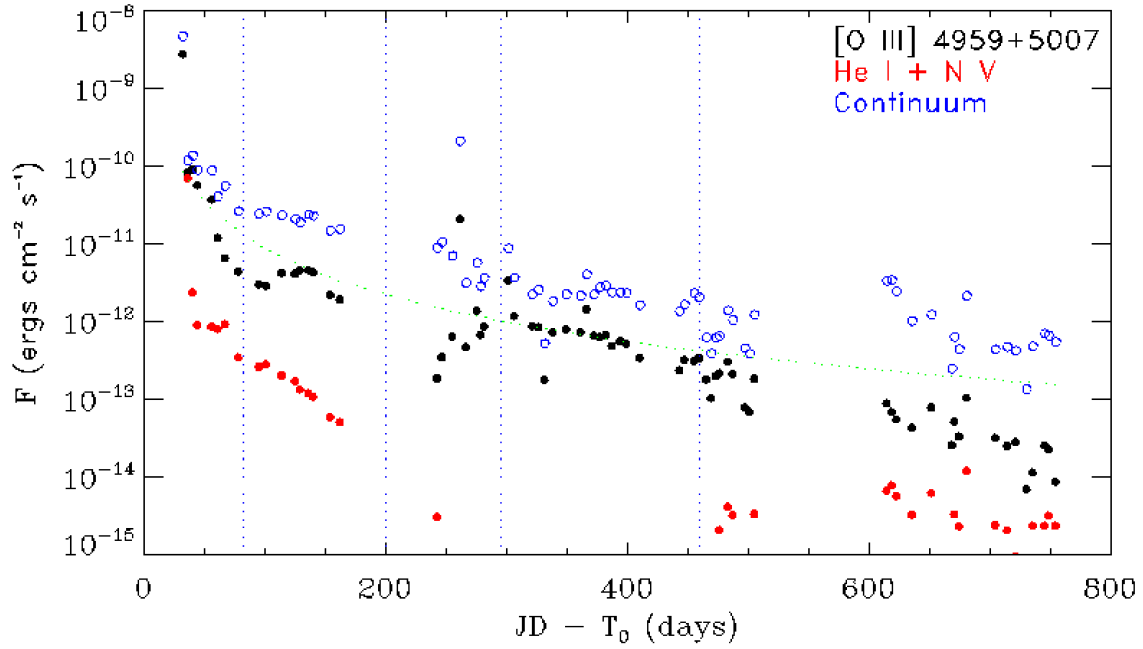
$$L_{V,\text{ff,wind}} = A_{\text{ff}} \frac{\dot{M}_{\text{wind}}^2}{v_{\text{ph}}^2 R_{\text{ph}}}. \quad (2)$$

This V flux represents the flux of free-free emission from optically thin plasma just outside the photosphere, and \dot{M}_{wind} is the wind mass-loss rate, v_{ph} the velocity at the photosphere, and R_{ph} the photospheric radius. See [Hachisu et al. \(2020\)](#) for the derivation of this formula and the coefficient A_{ff} . In our V light curve model, the total V band flux is defined by the summation of the free-free (FF) emission luminosity and the V band flux of the photospheric luminosity $L_{\text{ph,WD}}$ (assuming blackbody (BB)), i.e., FF+BB,

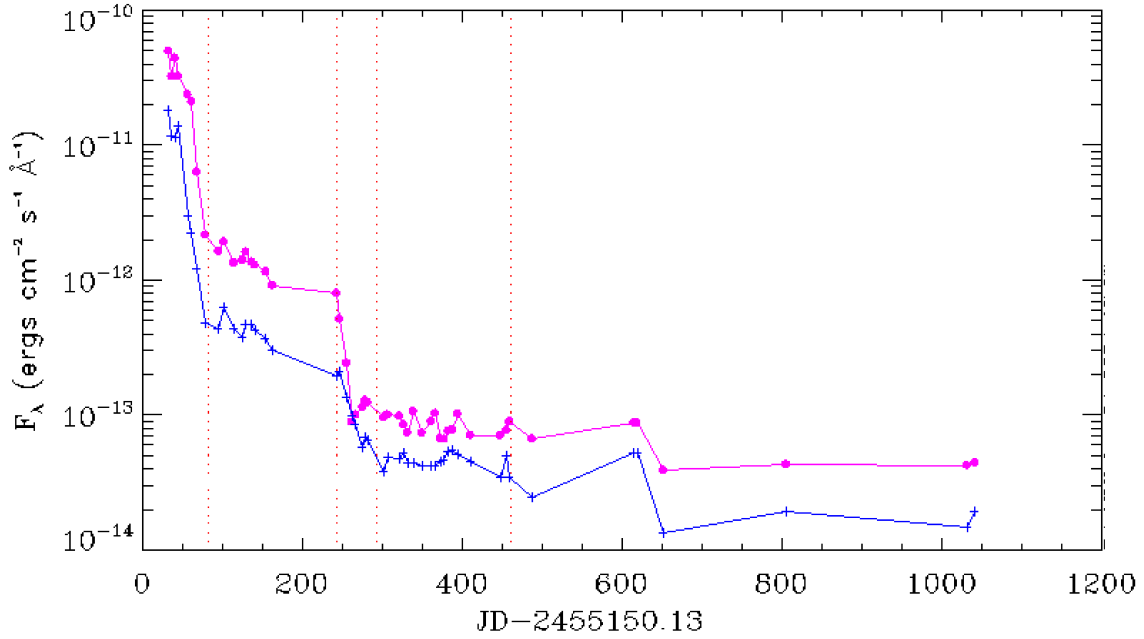
$$L_{V,\text{total}} = L_{V,\text{ff,wind}} + L_{V,\text{ph,WD}}. \quad (3)$$

The photospheric V band luminosity of the WD is calculated from a blackbody with T_{ph} and L_{ph} using a canonical response function of the V band filter, where T_{ph} and L_{ph} are the photospheric temperature and luminosity, respectively.

The winds are called ‘‘optically thick winds,’’ because matter is accelerated deep inside the photosphere ([Bath](#)



(a) Continuum (blue), [O III] (black), and He I+N V (red) fluxes in the V band



(b) Intensities of He II line (magenta) and continuum (blue)

Figure 3. The fluxes of emission lines and continuum of KT Eri calculated from the SMARTS spectra (Walter et al. 2012). The first two vertical dotted lines represent the period of the first plateau while the second two vertical dotted lines do that of the second plateau. (a) Temporal flux variations of continuum (blue), [O III] 4959Å + 5007Å lines (black), and He I 4922Å + N V 4945Å lines (red) in the V band (see, e.g., Williams 2012, for emission lines of novae). The continuum flux dominates the line fluxes at every time. T_0 is the time at maximum brightness (JD 2,455,150.13). (b) Temporal intensity variations of continuum (blue) and He II 4686Å line (magenta).

1978; Ruggles & Bath 1979; Kato & Hachisu 1994). Note that the wind itself becomes optically thin outside the photosphere. Free-free emission comes from optically-thin plasma outside the photosphere. Therefore, this free-free luminosity is not limited by the Eddington luminosity because the Eddington luminosity can be applied only to the optically-thick region.

We have estimated the WD mass by directly comparing the model light curves (e.g., Hachisu & Kato 2015, 2016a) with the observation. See Appendix A for details of this light curve model. Figure 1a shows the SMEL, V , and y light curves that show almost the same decline toward the quiescent phase. By comparing the KT Eri V, y light curves with a large number of model light curves in Hachisu & Kato (2006, 2015, 2016a, 2018) and Hachisu et al. (2020), we chose a best-fit model, which is plotted in Figure 1b (black line: $1.3 M_{\odot}$ WD model). Its WD mass is $1.3 M_{\odot}$, being consistent with the WD mass estimated from the position of KT Eri in the MMRD diagram (Figure 2). When free-free emission dominates the spectrum, both the V and y light curves show essentially the same decline along with our model light curve, until day ~ 40 , as in Figure 1b.

Our basic nova evolution is governed by a time-evolutionary sequence of the decreasing envelope mass of

$$\frac{d}{dt}M_{\text{env}} = \dot{M}_{\text{acc}} - \dot{M}_{\text{wind}} - \dot{M}_{\text{nuc}}, \quad (4)$$

where M_{env} is the mass of a hydrogen-rich envelope on the WD, \dot{M}_{acc} the mass accretion rate onto the WD, \dot{M}_{nuc} the mass decreasing rate of hydrogen-rich envelope by nuclear (hydrogen) burning, and usually $\dot{M}_{\text{acc}} \ll \dot{M}_{\text{wind}}$, and $\dot{M}_{\text{acc}} \ll \dot{M}_{\text{nuc}}$ for typical classical novae (see, e.g., Hachisu & Kato 2006). Therefore, the envelope mass is decreased by winds and nuclear burning. A large amount of the envelope mass is lost mainly by winds because of $\dot{M}_{\text{wind}} \gg \dot{M}_{\text{nuc}}$ in the early phase of nova outbursts (see Equation (7) of Hachisu & Kato (2006) for details). These FF+BB model light curves broadly follow the V, y light curves for the distance modulus in the V band of $(m - M)_V = 13.4$ until day ~ 30 –40, where the nebular phase started.

2.4. Same decline trend in the V and y light curves

In Figure 1a, the V and y light curves similarly decline and never depart from each other. This is a remarkable property of KT Eri, because many novae show large brightness difference between V and y magnitudes in the nebular phase, in which strong emission lines such as [O III] 4959, 5007 Å contribute to the wide V band flux. On the other hand, the intermediate Strömgren y band is designed to avoid such strong emission lines (see e.g., Figure 1 of Munari et al. 2013a). Thus,

the V magnitude is brighter than the y magnitude in the nebular phase, (see, e.g., Lockwood & Millis (1976) for V1500 Cyg, Gallagher et al. (1980) for V1668 Cyg, and Munari et al. (2015) and Hachisu et al. (2024) for V339 Del).

Figure 3a shows temporal flux variations of the continuum (blue open circles), [O III] 4959, 5007 Å (black dots), and He I 4922Å +N V 4945Å (red dots) of KT Eri in the V band, all of which are calculated from the SMARTS spectra of KT Eri (Walter et al. 2012). Here, we confirm that, in the V band of KT Eri, the fluxes of emission lines such as [O III] are not larger than the continuum flux. The continuum flux in the V band always dominates over each line flux in the V band. This supports our explanation that the V and y magnitudes do not depart from each other.

Although we see no clear indication of nebular phase in the light curve, there is a sign in the color-magnitude diagram of the KT Eri 2009 outburst (see Figure 12b). The start of the nebular phase can be detected as a turning point of the track, that is, from the bluest peak of the color index $B - V$ (e.g., Hachisu & Kato 2021, for such an example). The minimum (bluest) $B - V$ color was observed on day 39 (Imamura & Tanabe 2012). We regard the starting time of the nebular phase as day ~ 40 , which is indicated by the downward arrow labeled “nebular phase” in Figure 1b. The definition of color $B - V$ turning point is not the same as the definition of the start of nebular phase (e.g., [O III]/H $\beta > 1$), but the both dates are broadly coincident with each other in several novae, as later explained in Appendix C.5.

Hachisu & Kato (2022) theoretically showed that a strong shock inevitably arises far outside the photosphere in the post-maximum phase of a nova. In Kato et al. (2022a)’s nova model, the photospheric wind velocity decreases with time before optical maximum, but turns to increase after the optical maximum, so that the wind ejected later catches up with the wind ejected earlier and drives a shock. Thus, a strong shock naturally arises far outside the photosphere after the optical maximum. The mass of the shocked shell increases with time and reaches about 90% of the total ejecta mass. In other words, a large part of nova ejecta is eventually confined to the shocked shell. Therefore, the shocked shell becomes a main source of strong emission lines (e.g., Hachisu et al. 2024).

In KT Eri, however, these emission lines are not so strong compared with the continuum flux, because the continuum flux is rather high as depicted in Figure 3a. The flux of the continuum is always larger than those of strong emission lines such as [O III] and He I+N V in the V band. We will clarify the reason why the continuum

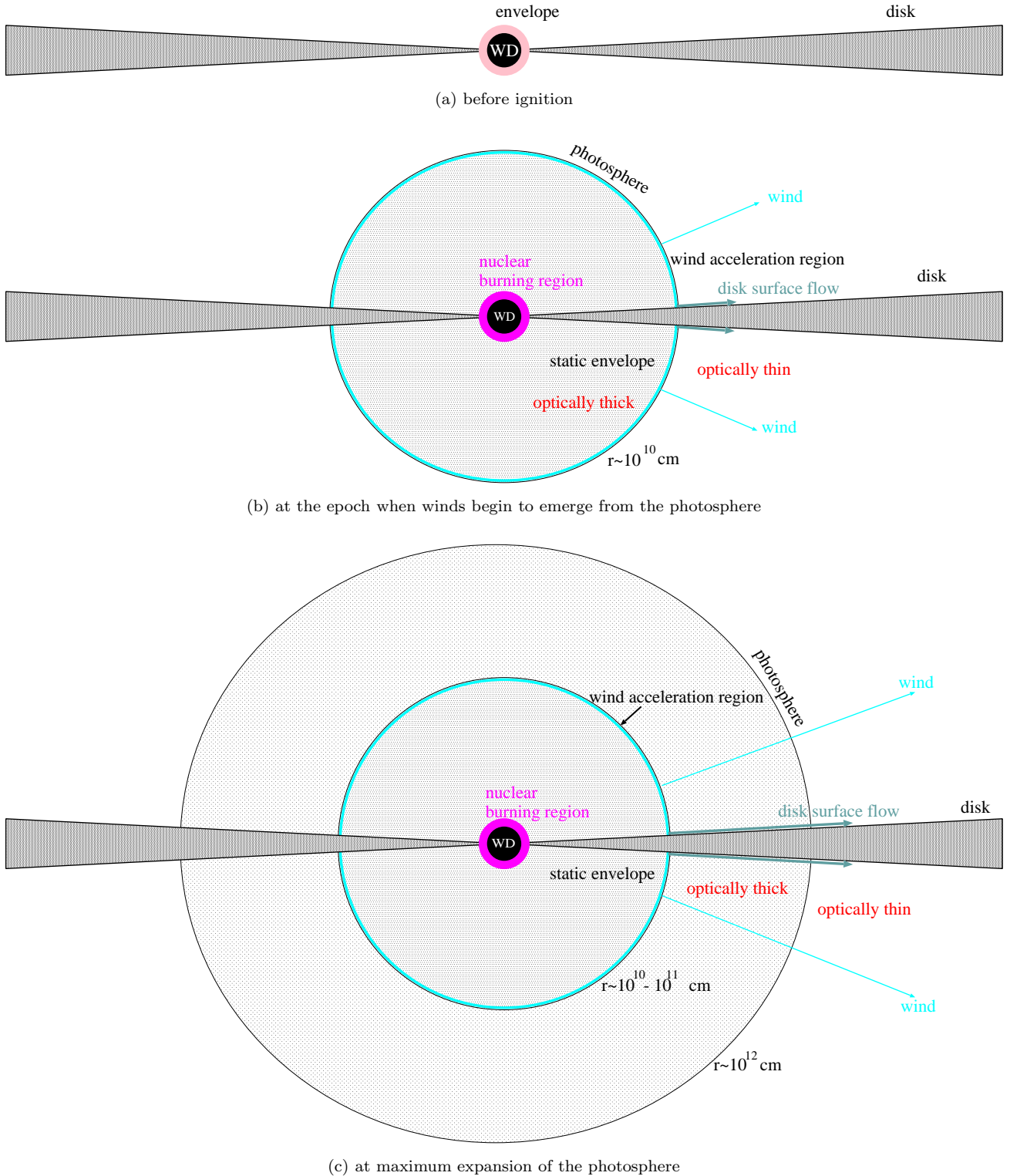


Figure 4. Schematic configurations of a WD envelope and accretion disk during a nova outburst: (a) before ignition of hydrogen burning; (b) at the epoch when winds begin to emerge from the photosphere; (c) at the maximum expansion of the photosphere. Optically thick winds have an opening angle avoiding the accretion disk. The spherical nova envelope configurations are taken from the spherically symmetric $1.3 M_{\odot}$ WD model in Figure 6 of Kato et al. (2024). The thick light-cyan region describes the acceleration region of winds. The dark-cyan arrows represent the disk surface (boundary layer) flows, which exist near the surface of accretion disk and have slower outflow velocities than those of winds.

flux always dominates each emission line flux later in this subsection and in Section 2.5.

Figure 1b shows that our model light curve (black line: FF+BB=continuum flux of free-free emission plus photospheric blackbody emission in Equation (3)) decays more rapidly than the V, y light curves after day ~ 40 . This is because, in our model, the wind mass-loss rate \dot{M}_{wind} rapidly drops after day ~ 40 . Thus, there should be additional optical sources, which are not line emissions because the y light curve does not depart from the V light curve. This continuum emission source should be optically-thick. We regard that this additional source is a photospheric emission of an equatorial, optically-thick disk.

The optically-thick winds are accelerated by the radiation pressure gradient deep inside the photosphere. Figure 4 shows this “acceleration region of winds.” The thick light-cyan circular lines in the figure correspond to this acceleration region of winds. The envelope is almost static (very low velocity) inside the acceleration region (Kato et al. 2022a, 2024). Therefore, we may conclude that the accretion disk is almost intact inside the acceleration region. The radius of the acceleration region is about $r_{\text{accel}} \sim 0.1 R_{\odot} \sim 10^{10}$ cm when winds start to emerge from the photosphere but expands up to $r_{\text{accel}} \sim 1 R_{\odot} \sim 10^{11}$ cm at maximum expansion of the photosphere (Figure 4c). The momentum of wind is spherically radial so that it does not so push the accretion disk outward because it has already an open angle avoiding the disk inside the acceleration region. The very thin surface layer can be blown in the wind (disk surface flow) and the disk expands over the Roche lobe size (Hachisu & Kato 2003a,b,c). Thus, we suppose that the accretion disk is almost intact, at least, from the view point of spherically radial momentum. However, it should be noted that the disk is embedded in radiation field and could be influenced in a thermal timescale.

We suppose that the interaction between two fluids (nova wind and accretion disk) causes a Kelvin-Helmholtz instability and effectively add radial momentum to a surface layer of the accretion disk. This can accelerate a disk surface flow up to ~ 1000 km s $^{-1}$, because the nova winds have velocities of $\sim 2000 - 3000$ km s $^{-1}$.

We assume that the disk is an accretion disk. This means that the mass is supplied by the companion star because the nova wind has an opening angle as explained in Figure 4b and c, and L1 point is not directly impacted by the nova wind.

In the nova wind phase, the surface layer of the disk is blown in the wind (e.g., Kelvin-Helmholtz instabil-

ity) and its photospheric surface can extend over the Roche lobe size of the WD. Such examples had been calculated to reproduce the light curves of SSSs (e.g., Hachisu & Kato 2003a,b,c). A strong support for the existence of a large accretion disk appeared in the eclipse analysis of the U Sco 2022 outburst. Muraoka et al. (2024) obtained a large disk (optically thick part) which is extended up to the L1 point, that is, the size is $\alpha \sim 1.3$ times the effective Roche lobe radius² of the WD during the nova wind phase. The disk (optically thick part) shrinks down to $\alpha \sim 0.85$ times the effective Roche lobe radius after winds stop. Here, α is the parameter that represents the size of the disk in units of the effective Roche lobe radius (see Equation (B1)). This issue will be described in more detail in Appendix B.

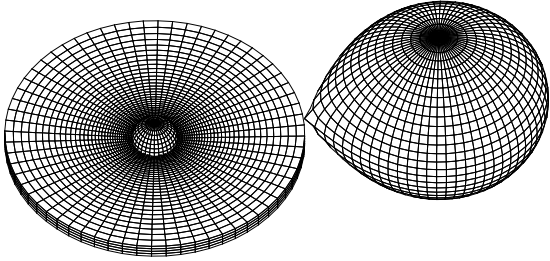
Assuming a large disk (Figure 5a), the size of which is 1.3 times the effective Roche lobe radius ($\alpha = 1.3$), we calculated the model light curve, as shown by the thick magenta line in Figure 1b, which can be written by the summation of the free-free emission luminosity and V band fluxes of the photospheric luminosities, i.e.,

$$L_{V,\text{total}} = L_{V,\text{ff,wind}} + L_{V,\text{ph,WD}} + L_{V,\text{ph,disk}} + L_{V,\text{ph,comp}}, \quad (5)$$

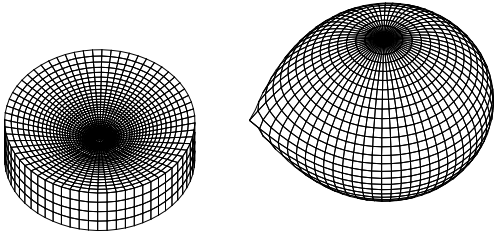
where $L_{V,\text{ph,disk}}$ is the V band flux from the disk, and $L_{V,\text{ph,comp}}$ the V flux from the companion star. The irradiation effect is the main optical source in the disk and companion star. See Appendix B.3 for detail of our irradiation calculation. The thick magenta line in Figure 1b shows a much slower decline than the black line, and broadly follows the V, y light curve until the SSS phase started.

We have examined the dependency of the model V light curve on the parameter α . Figure 1b shows the two cases of $\alpha = 1.3$ and 0.9. Here, $\alpha = 1.3$ (magenta line) is taken from Muraoka et al. (2024)’s result for U Sco, and $\alpha = 0.9$ (cyan-blue line) is close to the tidal limit of an accretion disk. The two light curves are very similar because the large orbital period of KT Eri (2.6 days) already allows a geometrically large disk even for $\alpha = 0.9$. The irradiated large disk substantially contributes to the total brightness. If we further increase α , the model V light curve hardly become brighter than the case of $\alpha = 1.3$. We interpret that the quick change in the size of the disk is caused by the quick weakening (or stop) of optically-thick winds. This issue will be discussed in Section 3.2.3.

² The effective Roche lobe radius is defined by the radius of a sphere of which the volume is the same as that of the inner critical Roche lobe. We adopt an approximate description proposed by Eggleton (1983).



(a) optically thick wind phase



(b) mass accretion makes a spray

Figure 5. Our light curve model of the disk around the WD of KT Eri in Figure 1b. The masses of the WD and Roche-lobe-filling companion star are $1.3 M_{\odot}$ and $1.0 M_{\odot}$, respectively. The orbital period is $P_{\text{orb}} = 2.616$ days. The inclination angle of the binary is $i = 41.2^{\circ}$. The separation is $10.55 R_{\odot}$ while their effective Roche lobe radii are $4.24 R_{\odot}$ and $3.76 R_{\odot}$, respectively. We assume, in panel (a), the size of the disk to be 1.3 times the Roche-lobe radius of the WD and the height of the disk edge to be 0.05 times the disk size during the nova wind phase but, in panel (b), the disk size is 0.9 times the Roche-lobe radius and the edge height is 0.3 times the disk size after the winds stop. The photospheric surfaces of the disk and companion star are irradiated by the central hot WD and such irradiation effects are all included in the calculation of the V light curve reproduction (see Hachisu & Kato 2001, for the partition of each surface and calculation method of irradiation). Note that, in panel (a), the disk surface flow matter in Figure 4 shapes an optically-thick large disk. A segment of mesh surface on the disk represents the photospheric surface of optically-thick part of the large disk. Gas is optically thin outside the mesh surfaces (i.e., photospheres of the disk, WD, and companion star). In panel (b), a photospheric surface of the disk shrinks inside the Roche lobe after the nova wind stops. The L1 stream impacts the disk edge and makes a spray, which elevates the disk edge (Schandl et al. 1997). We also include the effect of viscous heating in the accretion disk for a given mass-accretion rate (Hachisu & Kato 2001).

2.5. First plateau in the optical light curve

Figure 1b shows that the V, y brightnesses keep almost a flat plateau in the SSS phase (day ~ 80 –240). Because the wind from the WD weakened and stopped by day ~ 100 in our $1.3 M_{\odot}$ WD model (solid thick black line), the large disk comes back to a normal size, i.e., the edge of the disk shrinks inside the Roche lobe (see, e.g., Figure 5 of Muraoka et al. 2024). Assuming a disk size of 0.9 times the effective Roche lobe radius, we calculated the model light curve, as shown by the thick magenta line in Figure 1b. This thick magenta line reproduces a flat plateau until the hydrogen burning ends on day ~ 240 .

The end day of hydrogen shell-burning can be detected from the quick decay of He II 4686Å line intensity as well as the rapid decay of soft X-ray count rate. We plot the intensities of He II 4686Å line (magenta line) and continuum (blue line) in Figure 3b, which are calculated from the SMARTS spectra of KT Eri (Walter et al. 2012). Its flux quickly decays from day ~ 240 to day ~ 260 . This indicates that the high energy photons, which excite He II line, quickly decreases from day ~ 240 to day ~ 260 . Thus, hydrogen-shell burning ended on day ~ 240 and its soft X-ray or UV flux started to decay.

Such an optical plateau in the SSS phase is frequently observed in recurrent novae like in U Sco, the origin of which is explained by the contribution of an irradiated large accretion disk (e.g., Hachisu et al. 2000). An optical plateau, however, rarely appears in classical novae. Many classical novae are short (a few to several hours) orbital period binaries (e.g., Schaefer 2022a) and, thus, they have a small size disk that hardly contributes to the optical magnitude. Among classical novae, KT Eri is a rare exception of a long (as long as 2.6 days) orbital period (Schaefer et al. 2022), and could have a large disk. The disk model in the SSS phase will be explained in more detail in Appendix B.

2.6. Second plateau: high mass-accretion rate

At the end of the nova outburst, the optical magnitude quickly decays with the X-ray flux because hydrogen burning ends and the bright irradiation effect disappears, although our model includes irradiation effects of the accretion disk and companion star all the time during our simulation. To explain the brightness of the second plateau in KT Eri ($V \sim 14.1$), we assume a high mass-accretion rate of $\dot{M}_{\text{acc}} = 2 \times 10^{-7} M_{\odot} \text{ yr}^{-1}$, similar to the value estimated by Schaefer et al. (2022). Note that Schaefer et al.'s estimate of $\dot{M}_{\text{acc}} = 3.5 \times 10^{-7} (d/5.1 \text{ kpc})^2 M_{\odot} \text{ yr}^{-1}$ is converted to $\dot{M}_{\text{acc}} = 2 \times 10^{-7} M_{\odot} \text{ yr}^{-1}$ for $d = 4.2 \text{ kpc}$. The model light curve (thick magenta line in Figure 1b) shows the case of such a high mass-accretion rate. We include the effect

of viscous heating, the method of which is described in Hachisu & Kato (2001). Viscous heating in the accretion disk contributes to the brightness of $V \sim 14.1$ (see Table 1).

Our assumed mass-accretion rate of $\dot{M}_{\text{acc}} = 2 \times 10^{-7} M_{\odot} \text{ yr}^{-1}$ is close to the lowest mass-accretion rate for steady hydrogen burning, $\dot{M}_{\text{steady}} \approx 3 \times 10^{-7} M_{\odot} \text{ yr}^{-1}$, for a $1.3 M_{\odot}$ WD (see, e.g., Wolf et al. 2013; Kato et al. 2014, for recent estimates). If such a high mass-accretion rate continues in the SSS phase, hydrogen burns longer because new fuel is supplied. The SSS phase can be extended up to day ~ 240 , which is consistent with the duration of the observed SSS phase. If we assume a much smaller mass accretion rate of $\dot{M}_{\text{acc}} = 1 \times 10^{-9} M_{\odot} \text{ yr}^{-1}$, on the other hand, the hydrogen burning stops earlier on day ~ 180 (red line in Figure 1b) and the V brightness is $V \sim 15.3$ at the second plateau (Table 1). Thus, we can explain both the brightness in the second plateau ($V \sim 14.1$) and the SSS duration (until day ~ 240), at the same time, with a single mass accretion rate of $\dot{M}_{\text{acc}} = 2 \times 10^{-7} M_{\odot} \text{ yr}^{-1}$.

2.7. Brightness in the quiescent phase: Variable mass-accretion rate

The quiescent brightness of KT Eri is highly variable around at $V \sim 15.1$ ($V = 14.1 - 15.8$: Schaefer et al. 2022) after the outburst. The mean brightness of $V \sim 15.1$ can be reproduced with our model with the mass accretion rate of $\dot{M}_{\text{acc}} = 1 \times 10^{-8} M_{\odot} \text{ yr}^{-1}$ (Table 1). We suppose that the mass accretion rate had dropped from $\sim 2 \times 10^{-7} M_{\odot} \text{ yr}^{-1}$ to $\sim 1 \times 10^{-8} M_{\odot} \text{ yr}^{-1}$ ($V = 15.1$) or to $\sim 1 \times 10^{-9} M_{\odot} \text{ yr}^{-1}$ ($V = 15.3$) at the end of the second plateau phase, as depicted by the blue line with an arrow in Figure 1b.

Schaefer et al. (2022) raised the question on the origin of a large amplitude variation in quiescence. Our quick analysis shows that a brightness variation between $V \sim 14.1$ and $V \sim 15.8$ could be resulted from a large variation in the mass accretion rate between $\dot{M}_{\text{acc}} = 2 \times 10^{-7} M_{\odot} \text{ yr}^{-1}$ and $\dot{M}_{\text{acc}} = 1 \times 10^{-11} M_{\odot} \text{ yr}^{-1}$ (or virtually zero; see gray line in Figure 1b and Table 1). We indicate such a variation by the blue line with arrows in Figure 1b, although the origin of this large variation of mass transfer rate is unknown. We should note that the photospheric temperature of the companion star to be as low as 4,500 K, which is much lower than Schaefer et al. (2022)'s estimate of 6,200 K. We discuss more details of the brightness change in Appendix B.6.

2.8. Short summary of binary parameters

To explain the temporal variation of SMEI, V , and y light curves of KT Eri, we adopt the distance to KT Eri $d = 4.2$ kpc, reddening $E(B - V) = 0.08$ (Ragan et al. 2009), distance modulus in the V band $(m - M)_V = 13.4$, WD mass $M_{\text{WD}} = 1.3 M_{\odot}$, companion mass $M_2 = 1.0 M_{\odot}$ (Schaefer et al. 2022), surface temperature of the companion $T_{\text{ph},2} = 4,500$ K, separation $a = 10.55 R_{\odot}$, Roche lobe effective radii $R_{\text{RL},1} = 4.24 R_{\odot}$ and $R_{\text{RL},2} = 3.76 R_{\odot}$, inclination angle $i = 41.2^{\circ}$ for $K_{\text{WD}} = K = 58.4 \text{ km s}^{-1}$ (Schaefer et al. 2022), and orbital velocities $v_1 = 88.68 \text{ km s}^{-1}$ and $v_2 = 115.3 \text{ km s}^{-1}$, and orbital period $P_{\text{orb}} = 2.616$ days (Schaefer et al. 2022). The mass transfer rate from the companion star keeps a high value of $\dot{M}_2 \sim -2 \times 10^{-7} M_{\odot} \text{ yr}^{-1}$ until the second plateau ends, and then sometimes decreases down to virtually zero (no mass accretion), sometimes goes up to $\dot{M}_{\text{acc}} \sim 1 \times 10^{-7} M_{\odot} \text{ yr}^{-1}$, but its average is $\dot{M}_{\text{acc}} \sim 1 \times 10^{-8} M_{\odot} \text{ yr}^{-1}$ for $V \sim 15.1$, or $\dot{M}_{\text{acc}} \sim 1 \times 10^{-9} M_{\odot} \text{ yr}^{-1}$ for $V \sim 15.3$.

The surface of the accretion disk is blown in the wind. We also adopt the assumption that its optically thick part of the surface could be extended up to close to the L1 point, that is, 1.3 times the Roche lobe size during the nova wind phase, similar to what was found observationally for U Sco. When nova winds stop, its outer size shrinks down to 0.9 times the Roche lobe size, close to the tidal limit of an accretion disk. Then, the bright irradiation effects of the disk and companion star reproduce the brightness of the first plateau ($V \sim 12.0$) and the viscous heating of the disk ($\dot{M}_{\text{acc}} \sim 2 \times 10^{-7} M_{\odot} \text{ yr}^{-1}$) explains the brightness ($V \sim 14.1$) in the second plateau.

3. DISCUSSION

3.1. Is KT Eri a recurrent nova?

Schaefer et al. (2022) estimated the mass-accretion rate to the WD to be $3.5 \times 10^{-7} (d/5.1 \text{ kpc})^2 M_{\odot} \text{ yr}^{-1}$ from the brightness of an accretion disk and concluded that KT Eri is a recurrent nova with the recurrence time of 40–50 yr. In this subsection, we examine whether or not their conclusion is supported by our results.

Our model V light curves, together with variable $-\dot{M}_2$, suggest that (1) the mass-transfer rate ($-\dot{M}_2$) is as high as $2 \times 10^{-7} M_{\odot} \text{ yr}^{-1}$ in the first and second plateaus, but (2) $-\dot{M}_2$ drops to $1 \times 10^{-8} M_{\odot} \text{ yr}^{-1}$ for $V \sim 15.1$ or to $1 \times 10^{-9} M_{\odot} \text{ yr}^{-1}$ for $V \sim 15.3$ (Table 1), close to an average in the quiescent phase after the outburst. Here, \dot{M}_2 is the mass losing rate (negative) of the companion. If the total mass is conserved, we have $\dot{M}_{\text{acc}} + \dot{M}_2 = 0$. This lower mass-transfer rate is consistent with the suggestion from the MMRD position of KT

Eri (at $M_{\text{WD}} \sim 1.3 M_{\odot}$, $\dot{M}_{\text{acc}} \sim 1 \times 10^{-9} M_{\odot} \text{ yr}^{-1}$, and the recurrence time of $\sim 3,000 \text{ yr}$) in Figure 2. This decreasing tendency of mass-accretion rate in quiescence is also consistent with $\dot{M}_{\text{acc}} \approx 1.9 \times 10^{-10} (d/3.7 \text{ kpc})^2 M_{\odot} \text{ yr}^{-1}$ observed by Sun et al. (2020) about 8.3 yr after the outburst.

We should point out that, if we adopt the distance of $d = 4.2 \text{ kpc}$ instead of Schaefer et al.’s $d = 5.1 \text{ kpc}$, we have the mass-accretion rate of $\dot{M}_{\text{acc}} = 2 \times 10^{-7} M_{\odot} \text{ yr}^{-1}$ from their $3.5 \times 10^{-7} (d/5.1 \text{ kpc})^2 M_{\odot} \text{ yr}^{-1}$, which is consistent with our estimate during the second plateau. However, the average mass-accretion rate in quiescence becomes $\dot{M}_{\text{acc}} = 1 \times 10^{-8} M_{\odot} \text{ yr}^{-1}$, corresponding to the brightness variation from $V \sim 14.1$ (second plateau) to $V \sim 15.1$ (quiescence, average). Schaefer et al.’s very high \dot{M}_{acc} is probably valid only for the second plateau, but the mean mass-accretion rate in quiescence could be as low as $\sim 1 \times 10^{-9} M_{\odot} \text{ yr}^{-1}$ in a long interoutburst period as suggested by the position of KT Eri in Figure 2.

The estimated recurrence period is directly connected to the adopted mass-accretion rate. If we adopt the V brightness in quiescence before the outburst, $V_{\text{q,min}} = 15.3$, $\langle V_{\text{q}} \rangle = 14.5 \pm 0.2$, and $V_{\text{q,max}} = 14.0$ (Schaefer et al. 2022), the corresponding mass-accretion rate is calculated to be $\dot{M}_{\text{acc}} \sim 1 \times 10^{-9} M_{\odot} \text{ yr}^{-1}$, $\sim 1 \times 10^{-7} M_{\odot} \text{ yr}^{-1}$, and $\sim 2 \times 10^{-7} M_{\odot} \text{ yr}^{-1}$, as in Figure 1. These give us the recurrence times of 3600, 10, and 3.7 yr, respectively, for our $1.3 M_{\odot}$ WD (Hachisu et al. 2020). The estimated recurrence times do not change much for the other WD masses of 1.28 and $1.32 M_{\odot}$. The 10 and 3.7 yr recurrence times are not consistent with Jurdana-Šepić et al. (2012)’s results. This indicates that we cannot determine the recurrence time only from a short period observation in a much longer interoutburst duration.

Jurdana-Šepić et al. (2012) searched the archival plates of the Harvard College Observatory for a previous outburst of KT Eri, but found no outbursts between 1888 and 1962, and concluded that, even if KT Eri is a recurrent nova, it should have a recurrence time of centuries. This long recurrence time is also consistent with the suggestion ($\sim 3,000 \text{ yr}$) from the MMRD position of KT Eri in Figure 2 (and the 3600 yr from $V_{\text{q,min}} = 15.3$) but does not support both the 10 yr from $\langle V_{\text{q}} \rangle = 14.5 \pm 0.2$ and the 3.7 yr from $V_{\text{q,max}} = 14.0$. Thus, the mean brightness in a short timescale compared with a long interoutburst period has nothing on the mean mass-accretion rate to determine the recurrence period. All of these features consistently suggest that KT Eri is not a recurrent nova but its recurrence time is as long as $\sim 3,000 \text{ yr}$.

Finally, we compare the timescale of t_{peak} , the days from the outburst to optical maximum, between the observation and a theoretical model. We estimated the outburst day of KT Eri, from the rising trend in the SMEI light curve, to be $t_{\text{peak}} = 2.7$ days in Section 2. This estimate is broadly consistent with $t_{\text{peak}} = 2.5$ days for a self-consistent nova model of a $1.3 M_{\odot}$ WD with $\dot{M}_{\text{acc}} = 2 \times 10^{-9} M_{\odot} \text{ yr}^{-1}$ (model M13C10; Kato et al. 2024). The recurrence time of model M13C10 is about 1000 yr, also suggesting that KT Eri is not a recurrent nova.

3.2. Temporal changes of emission line profiles

We assumed a large disk during the nova wind phase in KT Eri (Section 2 and Appendix B). Here, we discuss whether or not the temporal changes of emission line profiles in KT Eri is consistent with our disk model in Figures 4 and 5.

3.2.1. Emission line profiles in the wind phase

Munari et al. (2014) reported spectroscopy of KT Eri between UT 2009 December 1 and UT 2014 February 14 (from day 19 to day 1553). They discussed the appearance and evolution of a narrow He II 4686Å emission line as well as Balmer lines of H α and H β . These lines show a narrow emission profile superimposed to much broader emission components. Figure 6b shows a schematic illustration of such two narrow and broad components.

Similar line profiles have been observed in other several novae, YY Dor, Nova LMC 2009, U Sco, DE Cir, and V2672 Oph (e.g., Munari et al. 2011; Mason et al. 2012; Mason & Munari 2014; Takeda & Diaz 2015, for spectra). These complex line profiles have always been modeled with asymmetric ejecta geometries, consisting of bipolar lobes, polar caps, and equatorial rings (see Ribeiro et al. 2013, for KT Eri).

Instead, in the nova wind phase, we interpret that the above narrow and broad line profiles come from a disk surface flow and spherically symmetric shocked shell, respectively.

Kato et al. (2022a) computed a nova outburst evolution including self-consistent wind mass-loss. Based on this result, Hachisu & Kato (2022) calculated a strong shock formation far outside the nova photosphere, and presented a configuration of the nova ejecta after the shock arose (Figure 6a). The shocked shell divides the ejecta into three parts, the earliest wind (before optical maximum), shocked shell, and inner wind. Hachisu & Kato (2022) interpreted that these three parts contribute to the three emission/absorption line systems defined by McLaughlin (1942), respectively, as illustrated in Figure 6a.

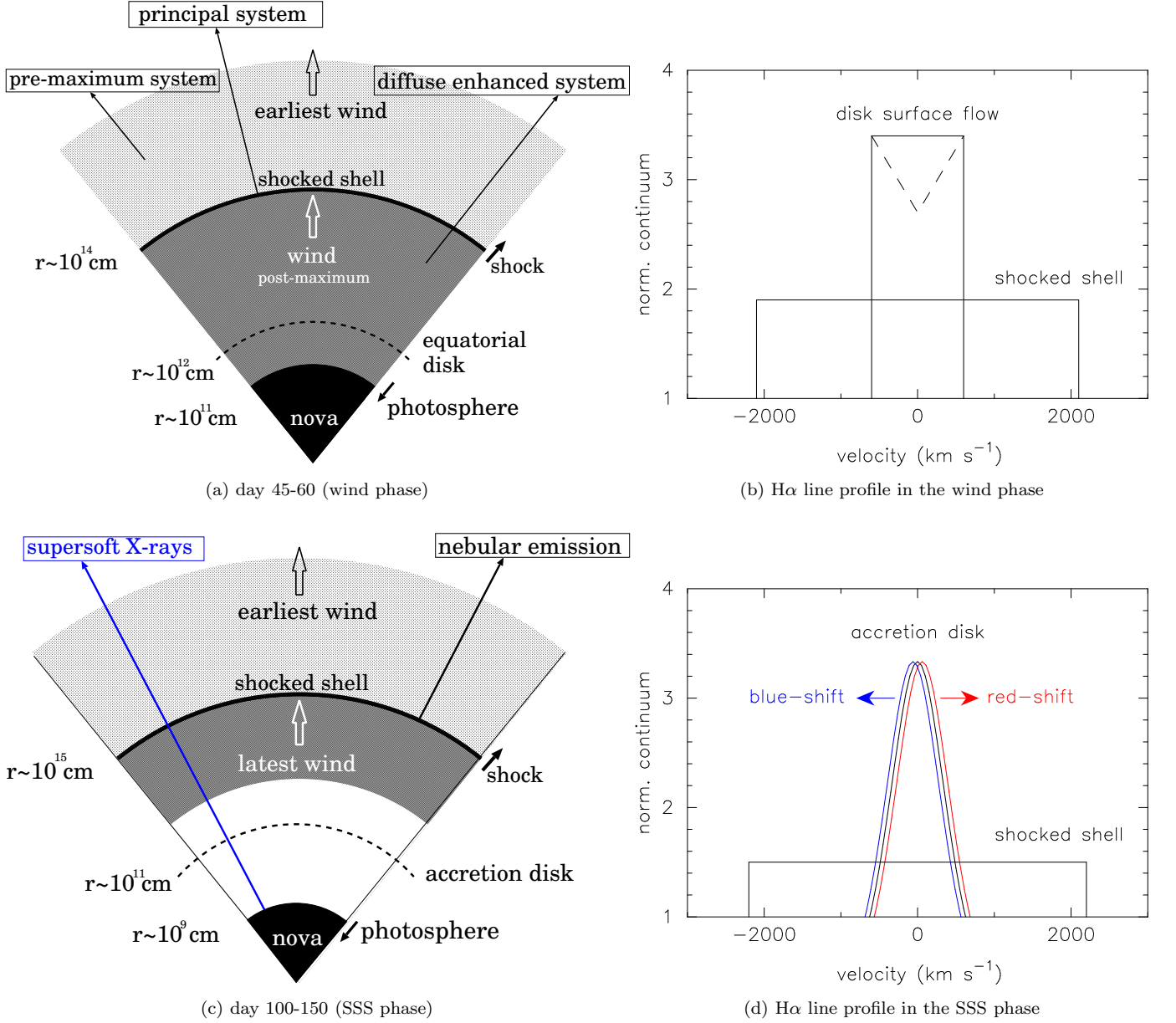


Figure 6. (a) Schematic illustration of a nova ejecta configuration in the wind phase of KT Eri (day $\sim 45 - 60$). The photosphere of the WD envelope has already shrunk to $R_{\text{ph}} \lesssim 1 R_{\odot}$ and an equatorial disk appears. A shock wave arose just after the optical maximum and has already moved far outside the WD photosphere (and the binary). The shocked shell emits Balmer lines such as $H\alpha$. The surface of the disk absorbs ultraviolet photons and becomes hot to emit $H\alpha$ photons. This figure is taken from Figure 2(b) of Hachisu & Kato (2023) with a modification. We assume that ejecta are spherically symmetric, but the disk is located on the orbital plane which is inclined with the angle of $i = 41.2^\circ$ from the line of sight. (b) Schematic $H\alpha$ line intensity profiles both from the disk surface flow (narrower component) and shocked shell (broader pedestal component). The shocked shell is geometrically thin, optically thin, and spherically symmetric, so its line profile is approximated by a rectangle with the line width of $v_{\text{exp}} = v_{\text{shock}} \sim 2100 \text{ km s}^{-1}$. The central narrower rectangular component is calculated from the outflowing disk surface flow with the velocity of $v_{\text{disk}} \sim 900 \text{ km s}^{-1}$ ($= 600 \text{ km s}^{-1} / \sin 41.2^\circ$) by assuming that the emissivity of $H\alpha$ is cylindrically uniform on the disk surface. These line profiles mimic the $H\alpha$ line profiles observed by Ribeiro et al. (2013). The dashed line mimics the effect of self-absorption. (c) Schematic illustration of a nova ejecta configuration in the SSS phase of KT Eri (on day $\sim 100 - 150$). The photosphere of the WD envelope has already shrunk to $R_{\text{ph}} \lesssim 0.1 R_{\odot}$ and emits supersoft X-rays. The shocked shell emits Balmer lines such as $H\alpha$ and other nebular lines. This figure is taken from Figure 2(d) of Hachisu & Kato (2023) with a modification. (d) Schematic line intensity profiles both from the accretion disk and shocked shell. The line profiles from the shocked shell are approximated by a rectangle with the line width of $v_{\text{exp}} = v_{\text{shock}} \sim 2,200 \text{ km s}^{-1}$. The central narrow line profiles mimic the line profile of the accretion disk with $\text{FWHM} \sim 1000 \text{ km s}^{-1}$ (taken from the $H\alpha$ line width in Munari et al. 2014). The line center moves along with the orbital motion.

The shocked shell is a bright source of $H\alpha$, because the shocked shell eventually collects $\sim 90\%$ of the nova ejecta mass (Hachisu & Kato 2022). If the shocked shell is spherically symmetric, geometrically thin, and optically thin, the $H\alpha$ profile is approximated by a rectangle (Beals 1931) with the width of $v_{\text{shell}} = v_{\text{shock}} \approx 2100 \text{ km s}^{-1}$, as illustrated in Figure 6b. Thus, the broader pedestal component should originate from the shocked shell with the velocity of $v_{\text{shell}} \sim 2100 \text{ km s}^{-1}$ in KT Eri.

It has been discussed that the sphericity (or elongation) of a nova shell depends on its (nova) speed class. The faster the nova speed class is, the more spherical the shell is (e.g., Downes & Duerbeck 2000). KT Eri belongs to the very fast novae class ($t_2 = 6.6$ days) and its shell is probably close to spherical. Therefore, our assumption of spherical symmetry does not so largely depart from the true shell.

The narrow components might arise from a disk surface flow in Figure 4c. This is because a thin surface layer of the disk is blown in the wind and its surface boundary flow has a smaller velocity than that of the wind itself (see more details in Appendix B.1). We calculated the narrower line profile, as in Figure 6b, a rectangle with the width of $v_{\text{incline}} \approx 600 \text{ km s}^{-1} = 900 \text{ km s}^{-1} \times \sin 41.2^\circ$, assuming a velocity of the disk surface flow in the radial direction, $v_{\text{disk}} = 900 \text{ km s}^{-1}$, where we adopt the inclination angle of $i = 41.2^\circ$ for the binary consisting of a $1.3 M_\odot$ WD and $1.0 M_\odot$ companion with the orbital period of $P_{\text{orb}} = 2.616$ days. We further assume circularly uniform emissivity distribution of $H\alpha$ on the disk surface. The concave or dip feature on the top could be due to self-absorption (dashed line in Figure 6b) because the boundary layer of disk surface flow is optically thick in the sense of line opacity, where $H\alpha$ lines come from.

Our narrow and wide component model for $H\alpha$ emission lines approximately reproduces the $H\alpha$ line profiles in KT Eri (see, e.g., Figures 2, 4–7 of Ribeiro et al. 2013).

3.2.2. Emission line profiles in the SSS phase

Figure 6c depicts a schematic configuration of the nova ejecta in the SSS phase of KT Eri. The optically-thick wind had already stopped emerging from the photosphere, but its tail still collides with the shock, and the WD photosphere emits supersoft X-ray photons.

Figure 6d shows a schematic illustration of the line profile in such a SSS phase: the line consists of a narrower Gaussian-like component and a broader pedestal component. The broader pedestal component originates from the shocked shell, as in the wind phase.

A strong shock arises outside the nova photosphere (Hachisu & Kato 2022, 2023), and propagate far beyond the binary orbit. Thus, the broader pedestal component of $H\alpha$ emission line hardly depends on the orbital phase. If the shocked shell is spherically symmetric, geometrically thin, and optically thin, the $H\alpha$ profile is a rectangle (Beals 1931) with the width of $v_{\text{shell}} = v_{\text{shock}} = 2,200 \text{ km s}^{-1}$, as illustrated in Figure 6d. Here, we assume that the shocked shell was accelerated from $v_{\text{shell}} = 2,100 \text{ km s}^{-1}$ in the wind phase to $v_{\text{shell}} = 2,200 \text{ km s}^{-1}$ in the SSS phase. See also the doublet [O III] line profiles of KT Eri obtained on day 294 by Arai et al. (2013), each component of which shows a broad $2,200 \text{ km s}^{-1}$ rectangular (pedestal) shape in the second plot of their Figure 2.

The narrow components might arise from the accretion disk of the binary (e.g., Sekiguchi et al. 1988, 1989; Thoroughgood et al. 2001; Walter & Battisti 2011) while a different interpretation on the narrow component of U Sco was proposed by Takeda & Diaz (2015). Here, we assume that the narrow component originates from the accretion disk because the disk is very bright due to an irradiation effect by the central hot WD (see more details in Appendix B). Although no broader pedestal components were observed, similar properties of narrow components of He II and Balmer emission lines are also observed in several persistent SSSs (e.g., Cowley et al. 1998; Schmidtke et al. 2000). Such a Gaussian-like line could be blue- or red-shifted by the orbital motion, as illustrated in Figure 6d, because narrow Gaussian-like He II or $H\alpha$ lines come from the irradiated accretion disk.

3.2.3. Transition from the wind phase to SSS phase

Munari et al. (2014) pointed out that the drastic change in the narrower component occurred on day ~ 70 from like Figure 6b to like Figure 6d. This can be explained if the disk configuration changes from Figure 5a to Figure 5b around on day ~ 70 (when the wind drastically weakened). In fact, Figure 3b shows the temporal variation of He II 4686\AA line intensity, in which the intensity (magenta line) quickly drops from $\sim 2 \times 10^{-11}$ to $\sim 2 \times 10^{-12} \text{ erg s}^{-1} \text{ cm}^{-2} \text{ \AA}^{-1}$ between day ~ 70 and ~ 90 . This 10 times drop in the intensity corresponds to both the shrinkage of the disk surface area and the rapid decrease in the wind mass-loss rate. Thus, our theoretical explanations of He II and Balmer emission lines are broadly consistent with Munari et al. (2014)'s observational results. Such a rapid shrinkage of the disk radius from $\alpha \sim 1.3$ to $\alpha \sim 0.85$ was observed ~ 25 days after optical maximum in the 2022 outburst of U Sco (see Figure 5 of Muraoka et al. 2024).

To summarize, the change from Figure 6b to Figure 6d is composed of two things: (1) One is that the broader pedestal component shows a gradual increase in the velocity (acceleration from 2,100 to 2,200 km s⁻¹) but a gradual decrease in the intensity over the transition from the wind phase to the SSS phase. This is consistent with our interpretation of shocked shell-origin, because the shocked shell is located far outside the binary and not directly related with the motion of binary. (2) The other is that the line profile of the narrower component drastically changes from the wind phase to the SSS phase. Moreover, the intensity of He II 4686Å emission line drops by a factor of 10 (Figure 3b). This drop in the intensity is consistent with both the rapid shrinkage in the surface area of the disk from the large disk to a normal size of the disk as well as the quick decrease in the wind mass-loss rate just before winds stop. Thus, the features of narrow Gaussian-like components of KT Eri are common among the several persistent SSSs (non novae), whereas the broader pedestal components appeared only in novae such as KT Eri. Persistent SSSs have no strong shocked shell, but their binary nature is similar to KT Eri in the SSS phase, i.e., like in Figure 5b.

4. CONCLUSIONS

Our main results are summarized as follows:

1. Our 1.3 M_{\odot} WD (Ne3) model well reproduces the SMEI, V , and y light curves of KT Eri. In our model, the V light curve consists of free-free (FF) emission from the wind just outside the photosphere plus blackbody (BB) emission from the WD photosphere. The supersoft X-ray flux (0.3-10.0 keV) is calculated from blackbody emission from the WD photosphere. The relatively long duration of supersoft X-ray source (SSS) phase can be explained by a relatively large mass-transfer rate of $-\dot{M}_2 \sim 2 \times 10^{-7} M_{\odot} \text{ yr}^{-1}$ in the SSS phase.
2. We obtain the distance modulus in the V band to be $\mu_V \equiv (m - M)_V = 13.4 \pm 0.2$ from the direct model light curve fitting for our 1.3 M_{\odot} WD (Ne3) model. This gives a distance of $d = 4.2 \pm 0.4$ kpc toward KT Eri for the observed reddening of $E(B - V) = 0.08$.
3. Both the V and y brightnesses decline almost in the same way even in the nebular phase. To explain the similar behaviors of V and y light curves in the later phase, we assume a large disk around the WD, temporally extended by strong nova winds, the radius of which is 1.3 times the effective Roche-lobe size, similar to what was found

observationally for U Sco. The brightness itself is not so sensitive to the size of the disk if the size is larger than 0.9 times the Roche lobe radius, because the disk is already large for such a long orbital period of 2.6 days. After the winds stop, we assume a normal size of the disk with an elevated edge. Both the disk and companion star are irradiated by the hot WD. The first plateau ($V \sim 12.0$) is reproduced with a bright disk irradiated by the hydrogen-burning hot WD.

4. The second plateau ($V \sim 14.1$) is explained by a viscous heating disk together with a high mass-transfer rate of $-\dot{M}_2 \sim 2 \times 10^{-7} M_{\odot} \text{ yr}^{-1}$. The V brightness drops to $V \sim 15.1$ (or $V \sim 15.3$) when the mass-transfer rate decreases to $-\dot{M}_2 \sim 1 \times 10^{-8} M_{\odot} \text{ yr}^{-1}$ (or $-\dot{M}_2 \sim 1 \times 10^{-9} M_{\odot} \text{ yr}^{-1}$) in quiescence.
5. The mass-accretion rate of $\dot{M}_{\text{acc}} = 2 \times 10^{-7} M_{\odot} \text{ yr}^{-1}$ is close to the lowest mass-accretion rate for steady hydrogen burning, $\dot{M}_{\text{steady}} \approx 3 \times 10^{-7} M_{\odot} \text{ yr}^{-1}$, for a 1.3 M_{\odot} WD. If such a high mass-accretion rate continues in the SSS phase, hydrogen burns longer because new fuel is supplied. The SSS phase can be extended up to day ~ 240 , being consistent with the duration of the observed SSS phase. Therefore, we can explain both the brightness in the second plateau ($V \sim 14.1$) and the SSS duration (until day ~ 240), at the same time, with a single mass accretion rate of $\dot{M}_{\text{acc}} = 2 \times 10^{-7} M_{\odot} \text{ yr}^{-1}$.
6. A large temporal brightness variation from $V \sim 14.0$ to $V \sim 15.8$ in quiescence can be explained as a variable mass-transfer rate from $-\dot{M}_2 \sim 2 \times 10^{-7} M_{\odot} \text{ yr}^{-1}$ to $-\dot{M}_2 \sim 1 \times 10^{-11} M_{\odot} \text{ yr}^{-1}$ (virtually zero mass-transfer rate) for the photospheric temperature $T_{\text{ph},2} \approx 4,500$ K of the companion star with $M_2 \approx 1.0 M_{\odot}$.
7. The recurrence time is difficult to estimate from the V brightness in quiescence, because its observational period is too short compared with a much longer interoutburst period. Instead, we estimate the recurrence period from the position of KT Eri in the MMRD diagram to be ~ 3000 yr.
8. We analyzed the temporal variation of H α line profiles based on our nova model as well as our binary model. The H α line consists of a broader pedestal component and a narrower component. The broader component originates from a spherically-symmetric, shocked shell with the line width of

$v_{\text{shell}} = 2,100\text{--}2,200 \text{ km s}^{-1}$. We interpret the narrower component as arising from the outflowing disk surface flow with the velocity of $v_{\text{disk}} = 900 \text{ km s}^{-1}$ in the wind phase. In the SSS phase after winds stop, the disk shrinks to a normal size and the narrower component becomes similar to that of persistent supersoft X-ray sources, the line center of which moves along with the orbital motion.

9. We apply the time-stretching method to the B , V , and I_C light curves of KT Eri, and obtain the distance moduli in the B , V , and I_C bands in Appendix C.1. The three different distance-reddening relations of $(m - M)_B = 13.47 \pm 0.2$, $(m - M)_V = 13.4 \pm 0.2$, and $(m - M)_I = 13.27 \pm 0.2$ cross roughly at the distance of $d = 4.2 \text{ kpc}$ and $E(B - V) = 0.08$, being consistent with the Gaia eDR3 distance of $d = 4.1^{+0.5}_{-0.4} \text{ kpc}$ (Bailer-Jones et al. 2021), Schaefer (2022b)’ esti-

mate $d = 4211^{+466}_{-296} \text{ pc}$, and the observed reddening of $E(B - V) = 0.08$ (Ragan et al. 2009).

10. The maximum V brightness of KT Eri is $M_V = -8.0$ for $(m - M)_V = 13.4$ and the decline rates in the SMEI ($\approx V$) light curve are $t_2 = 6.6$ and $t_3 = 13.6$ days (Hounsell et al. 2010). The positions of KT Eri in the maximum magnitude versus rate of decline ($t_2\text{-}M_{V,\text{max}}$ and $t_3\text{-}M_{V,\text{max}}$) diagrams for classical novae (Hachisu et al. 2020) are consistent with our $1.3 M_{\odot}$ WD (Ne3) model, of which the recurrence period and average mass accretion rate are $\sim 3,000 \text{ yr}$ and $\sim 1 \times 10^{-9} M_{\odot} \text{ yr}^{-1}$, respectively. Thus, we may conclude that KT Eri is not a recurrent nova.

We thank the Variable Star Observing League of Japan (VSOLJ) and the American Association of Variable Star Observers (AAVSO) for the optical photometric data of KT Eri and other novae. We are also grateful to the anonymous referee for useful comments that improved the manuscript.

APPENDIX

A. WHITE DWARF MODELS OF OPTICAL AND SUPERSOFT X-RAY LIGHT CURVES

We present multiwavelength light curves based on the optically thick wind model of novae and constrain the range of possible white dwarf (WD) masses. Hachisu & Kato (2006) calculated many free-free emission light curves for novae with various WD masses and chemical compositions based on Kato & Hachisu (1994)’s nova wind model. Our model V, y light curve is calculated from the summation of free-free (FF) emission from the model nova wind and blackbody (BB) emission from the model WD photosphere (Hachisu & Kato 2015). We name such a light curve model “FF+BB” (see Equations (2) and (3)). The absolute magnitude of each FF+BB model light curve has been calibrated with several novae with a known distance modulus in the V band (Hachisu & Kato 2015; Hachisu et al. 2020). This can be done by fixing the coefficient A_{ff} in Equation (2). These model light curves have reproduced the decay trends of various nova light curves. We chose appropriate models among the light curve database and select ones that fit reasonably to the observational light curve of KT Eri.

Figure 7 shows our selected models. Figure 7a shows the FF+BB model light curves of $1.23 M_{\odot}$ (blue

line), $1.26 M_{\odot}$ (black), $1.28 M_{\odot}$ (green), and $1.3 M_{\odot}$ (magenta) WDs for the chemical composition of Ne2 (Hachisu & Kato 2010), i.e., $X = 0.55$, $Y = 0.30$, $Z = 0.02$, $X_{\text{CNO}} = 0.10$, $X_{\text{Ne}} = 0.03$ by mass weight. Here, X , Y , and Z are the hydrogen, helium, and heavy element content, and X_{CNO} is the total abundance of extra carbon, nitrogen, and oxygen, and X_{Ne} the extra neon (e.g., Hachisu & Kato 2006). These optical fluxes are taken from Table 3 of Hachisu & Kato (2010). In Figure 7b, we choose another set of the chemical composition of Ne3, i.e., $X = 0.65$, $Y = 0.27$, $Z = 0.02$, $X_{\text{CNO}} = 0.03$, $X_{\text{Ne}} = 0.03$ (Hachisu & Kato 2016a), and plot three FF+BB model light curves of $1.28 M_{\odot}$ (blue), $1.3 M_{\odot}$ (black), and $1.32 M_{\odot}$ (green) WDs. We also add the corresponding X-ray light curves to the figure. Here, we assume that the mass-accretion rate to the WD is $\dot{M}_{\text{acc}} = 1 \times 10^{-9} M_{\odot} \text{ yr}^{-1}$ for all models.

Our model X-ray flux (0.3–10.0 keV) is calculated from the model WD photosphere with blackbody assumption for the photospheric temperature T_{ph} and photospheric radius R_{ph} (Kato & Hachisu 1994). Here, we neglect absorption for X-rays outside the photosphere. It should be noted that the X-ray flux is not the same as the X-ray count rate, although the X-ray model light curves broadly catch up the rising phase of the Swift X-ray count rate.

With the distance modulus in the V band $(m-M)_V = 13.4$, all the model V light curves broadly follow the V observation of KT Eri until each model light curve starts to bend downward. On the other hand, the rise of model X-ray light curve broadly catches up with the Swift X-ray observation, at least, for $M_{\text{WD}} = 1.3, 1.28,$ and $1.26 M_{\odot}$ (Ne2), in Figure 7a, but for $M_{\text{WD}} = 1.32, 1.3,$ and $1.28 M_{\odot}$ (Ne3), in Figure 7b. Here, we select each WD mass with the $\Delta M_{\text{WD}} = 0.02 M_{\odot}$ interval. The other WD mass models are excluded (by $\Delta M_{\text{WD}} = 0.02 M_{\odot}$ interval).

Figure 7 shows, however, that the model X-ray fluxes decay much earlier than the observed count rate for all of these models. To mitigate the difference, we examined how we extend the duration of hydrogen burning up to day ~ 240 , as in Figures 1b, with high mass-accretion rates of $\dot{M}_{\text{acc}} \gg 1 \times 10^{-9} M_{\odot} \text{ yr}^{-1}$. This will be described in Section B.7.

B. LIGHT CURVE MODELS OF ACCRETION DISK AND COMPANION STAR

We describe details of our irradiated disk and binary model for KT Eri. The large gap between our FF+BB model light curves and the V, y observation indicates a significant contribution from an irradiated disk. Here, we assume an accretion disk before nova explosion as in Figure 4a, of which the surface layer is blown in the nova wind after nova explosion (Figure 4b and c). This is a kind of disk winds in cataclysmic variables, which is driven by nova winds. When the disk surface flow (disk wind) is optically thick, its disk shape looks extending over the Roche lobe (Figure 5a). The photosphere of the large disk emits continuum blackbody flux. In the optically thick wind phase of a nova, matter is accelerated deep inside the photosphere. However, the wind itself becomes optically thin outside the photosphere. The density of the wind is rather low compared with that of the disk. We plot our model for a nova and accretion disk in Figure 4, the details of which are described in Appendix B.1. The binary parameters and disk parameters are already described in Section 2.8, but we reexamine them in Appendix B.2-B.8.

A bright irradiated disk has been studied in the several supersoft X-ray sources and recurrent novae (e.g., Schandl et al. 1997; Hachisu et al. 2000; Hachisu & Kato 2001, 2003a,b,c). When the disk is irradiated by the central hot WD, its surface temperature increases, and each part of the disk surface emits photons at this increased temperature. In our modeling, the size and shape of the disk are parameters. We also include the effect of viscous heating in the accretion disk (Hachisu & Kato 2001). Our model of such an irradi-

ated disk and companion star is given in Appendix B.3 and the composite model light curves are described in Appendix B.4-B.8.

B.1. *Disk is not disrupted by nova winds*

Kato et al. (2022a, 2024) presented nova outburst models that self-consistently include optically-thick winds as a mass-loss mechanism. We here show the reason why an accretion disk is not disrupted in a nova outburst based on Kato et al. (2024)'s nova model. In Figure 4, we show a schematic illustration of Kato et al.'s evolution model of a nova envelope for a $1.3 M_{\odot}$ WD, which is taken from their Figure 6. After hydrogen ignites at the bottom of the envelope (Figure 4a), the nova envelope expands almost hydrostatically until winds begins to emerge from the photosphere (Figure 4b). This phase can be detected as an X-ray flash because the temperature of the photosphere is high enough to emit supersoft X-rays. Such an X-ray flash was first detected by the SRG/eROSITA in the 2020 nova outburst of YZ Ret (König et al. 2022). The X-ray flash of YZ Ret is consistent with the nova outburst model of a $\sim 1.3 M_{\odot}$ WD (Kato et al. 2022b,c).

From the X-ray spectrum analysis of YZ Ret, König et al. (2022) found no major intrinsic absorption during the X-ray flash. Therefore, Kato et al. (2022b) concluded that

- (1) no dense matter exists around the WD photosphere,
- (2) no indication of a shock wave, and
- (3) the hydrogen-rich envelope is almost hydrostatic.

Note that all of these are consistent with Kato et al. (2024)'s theoretical model. We adopt their conclusions: optically-thick winds do not yet emerge from the photosphere at the epoch of X-ray bright (X-ray flash) phase and the envelope is almost hydrostatic. Thus, we conclude that the accretion disk is almost intact until winds begin to emerge from the photosphere (Figure 4b) because the envelope expands almost hydrostatically and the density of the accretion disk is much higher than that of the envelope.

With such information, we assume that the disk in the KT Eri system is also surviving during the nova outburst and a thin surface layer of the disk is blown in the wind. We call such a flow of the boundary layer between winds and disk the “disk surface flow.” The dark-cyan arrows indicate the disk surface flow, the velocity of which should be slower than that of a wind (Figure 4b and c). The outflowing disk matter shapes a large optically-thick disk.

The nova envelope further expands and, at the same time, blows winds (Figure 4c). The wind is accelerated deep inside the photosphere. For this reason, it is called

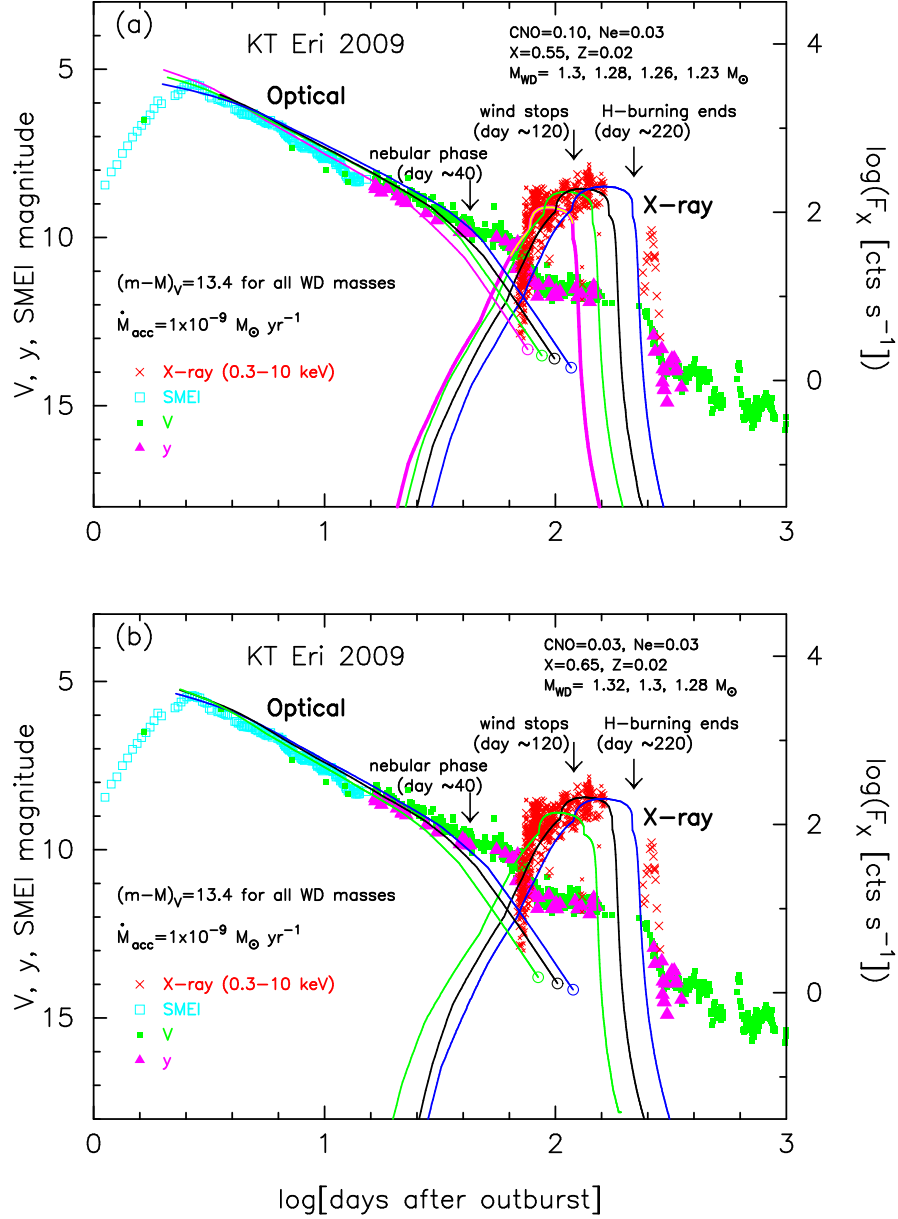


Figure 7. Same as Figure 1b, but we plot only FF+BB light curves and X-ray (0.3–10.0 keV) light curves for different sets of WD mass and chemical composition. The mass-accretion rate onto the WDs is fixed to be $\dot{M}_{\text{acc}} = 1 \times 10^{-9} M_{\odot} \text{ yr}^{-1}$. (a) Ne2: $1.23 M_{\odot}$ (blue line), $1.26 M_{\odot}$ (black), $1.28 M_{\odot}$ (green), and $1.3 M_{\odot}$ (magenta but yellow on the top part of X-ray). (b) Ne3: $1.28 M_{\odot}$ (blue), $1.3 M_{\odot}$ (black), and $1.32 M_{\odot}$ (green) WDs.

the “optically thick wind,” but winds become optically thin outside the photosphere as depicted in Figure 4c. The velocity of wind at the photosphere decreases as the photosphere expands (see Figure 6 of Kato et al. 2024). The wind mass-loss rate also reaches maximum at maximum expansion of the photosphere. At the same time, the free-free emission brightness also attains its maximum (optical maximum) because of Equation (2). A substantial part of the envelope is blown in the wind.

We plot the envelope structure at/near maximum expansion of photosphere in Figure 4c.

The winds are accelerated by the radiation pressure gradient deep inside the photosphere. We call this region the “acceleration region of winds.” The thick light-cyan circular lines in Figure 4b and c correspond to this acceleration region of winds. The envelope is almost static (very low velocity) inside the acceleration region (Kato et al. 2022a, 2024). Therefore, we may

conclude that the accretion disk is almost intact inside the acceleration region. The radius of the acceleration region is about $r_{\text{accel}} \sim 0.1 R_{\odot} \sim 10^{10}$ cm when winds start to emerge from the photosphere but expands up to $r_{\text{accel}} \sim 1 R_{\odot} \sim 10^{11}$ cm at maximum expansion of the photosphere (Figure 4c). The momentum of wind is spherically radial so that it does not so push the accretion disk outward because it has already an open angle avoiding the disk inside the acceleration region. Thus, we suppose that the accretion disk is almost intact, at least, from the view point of spherically radial momentum.

Drake & Orlando (2010) reported their 3D numerical calculations on the 2010 nova outburst of U Sco and concluded that the accretion disk is completely destroyed by the blast wave. However, Muraoka et al. (2024) observationally showed that a large size of the optically-thick light source exists during the nova wind phase, about 14 days after optical maximum, in the 2022 outburst of U Sco. They showed that the light source edge was extended close to the L1 point. They interpreted this as a structure change of the disk, the size of which is expanded to ~ 1.2 times the effective Roche lobe radius of the white dwarf component. The size of the optical source drastically shrinks to ~ 0.8 times the effective Roche lobe radius 26 days after optical maximum, close to the tidal limit of an accretion disk. This observational result and its interpretation are consistent with our model that only the outermost surface region of the disk is blown in the wind (disk surface flow) and the outer edge of the optically thick part of the disk is extended over the Roche lobe size (see, e.g., Hachisu & Kato 2003a,b,c).

Drake & Orlando (2010) set up their initial model by a spherical Sedov-type shock wave at the radius of $r_0 = 4 \times 10^5$ km = 4×10^{10} cm with the total energy of $E_0 \sim 10^{44}$ erg. This initial set-up is not supported by Kato et al. (2024)'s nova outburst model as shown in Figure 4c. Hachisu & Kato (2022) showed that a strong shock arises only after optical maximum (after maximum expansion of the photosphere). When the shock arises, this radius already expands to, typically, $r_0 \sim 10^{12} - 10^{13}$ cm or more. The separation of U Sco binary is about $a = 6.5 R_{\odot} \sim 0.5 \times 10^{12}$ cm, which is comparable to or smaller than the formation radius of a shock. In other words, a shock does not collide with the disk because the shock formation radius is outside the disk edge in the U Sco binary system. Hachisu & Kato (2022) also showed that, even if a strong shock arises and collides with the disk, it is a reverse shock, different from the Sedov-type shock. The reverse shock appears when the inner fast moving matter collides with

the outer slow moving matter, which therefore depends on the faster wind inside the shock (see, e.g., Figure 4 of Hachisu & Kato 2022). The inner wind has an open angle avoiding the disk, so that no spherical reverse shock arises in the accretion disk.

Thus, the numerical results by Drake & Orlando (2010) on the recurrent nova U Sco are not supported by both the observation (Muraoka et al. 2024) and the nova outburst models (Hachisu & Kato 2022; Kato et al. 2022a, 2024). Therefore, the dynamical impact of the fast outflow (optically thick wind) does not disrupt the disk in the early phase (until optical maximum).

We do not include any other effects that would be important for disk disruption. For example, a prolonged contact with the hot, quasi-hydrostatic envelope could lead to a thermal evaporation of a significant amount of disk material.

We have already assumed that the disk surface flows (disk winds) strip off a very thin surface layer of the disk. We suppose that this effect is the largest mass loss from the accretion disk (Figure 4b and c). Unfortunately, we cannot correctly estimate the mass-loss rate by disk surface flows. At the present time, therefore, we simply assume that the optically thick part of the disk surface flows remains during the nova wind phase and this large disk (shape) contributes to the V and y magnitudes as shown in Figure 1b. If we successfully reproduce the V and y magnitudes by this assumption of the large disk, we may conclude that a large disk could survive during the nova outburst of KT Eri.

B.2. Binary parameters

We have already obtained a parameter set of $M_{\text{WD}} = 1.3 M_{\odot}$ (Ne3) and $T_{\text{ph},2} = 4,500$ K for $M_2 = 1.0 M_{\odot}$ in Section 2.8, which reasonably well reproduced the V, y optical light curves as well as the X-ray light curve. However, we start here $M_{\text{WD}} = 1.28 M_{\odot}$ (Ne3) and $T_{\text{ph},2} = 6,200$ K for $M_2 = 1.0 M_{\odot}$, based on Schaefer et al. (2022)'s suggestion ($M_{\text{WD}} = 1.25 \pm 0.3 M_{\odot}$ and $T_{\text{ph},2} = 6,200$ K for $M_2 = 1.0 \pm 0.2 M_{\odot}$). For this set of parameters, the separation of the binary is $a = 10.5 R_{\odot}$, the effective radii of each Roche lobe are $R_{\text{RL},1} = 4.2 R_{\odot}$ and $R_{\text{RL},2} = 3.8 R_{\odot}$, the orbital velocity of the WD is $v_{\text{orb},1} = 89.2$ km s $^{-1}$, for the orbital period of $P_{\text{orb}} = 2.616$ days (Schaefer et al. 2022). We estimate the inclination angle of the binary to be $i = 40.9^{\circ}$ assuming that $K = 58.4$ km s $^{-1}$ is coming from the orbital velocity of the WD (Schaefer et al. 2022).

In what follows, we change M_{WD} and $T_{\text{ph},2}$ and examine whether or not the combination of M_{WD} and $T_{\text{ph},2}$

reproduces the V, y and X-ray light curves of KT Eri, as shown in Figure 1b.

B.3. Irradiated disk and companion star

We assume that the photosphere of the companion star just fills its Roche lobe as in Figure 5. We also assume that the disk surface is cylindrically symmetric around the WD. As already explained in Appendix B.1, a large disk represents the photosphere of the disk surface flow (disk winds), the radial velocity of which is as large as $\sim 1000 \text{ km s}^{-1}$ (see Section 3.2) because it is driven by the nova winds of velocities $v_{\text{wind}} \sim 2000 - 3000 \text{ km s}^{-1}$. Therefore, the disk surface flow is dynamical (much larger than the orbital velocity of $v_{\text{orb}} \sim 100 \text{ km s}^{-1}$) and does not need to follow the gravitational potential (or the Roche potential). It is reasonable that we assume axisymmetric flow when the nova wind is axisymmetric (or spherically symmetric).

The size of the disk is defined by

$$R_{\text{disk}} = \alpha R_{\text{RL},1}, \quad (\text{B1})$$

and the height of the disk at the edge is given by

$$H_{\text{disk}} = \beta R_{\text{disk}}. \quad (\text{B2})$$

The surface height z of the disk at the equatorial distance $\varpi = \sqrt{x^2 + y^2}$ from the center of the WD is assumed to be

$$z = \left(\frac{\varpi}{R_{\text{disk}}} \right) H_{\text{disk}}, \quad (\text{B3})$$

during the wind phase, but

$$z = \left(\frac{\varpi}{R_{\text{disk}}} \right)^2 H_{\text{disk}}, \quad (\text{B4})$$

after the winds stop.

Hachisu & Kato (2003a,b,c) proposed a large disk ($\alpha \sim 1.5 - 3.0$, $\beta = 0.05$) during the wind phase to reproduce the temporal variations of the V light curves of various supersoft X-ray sources (SSSs), such as the recurrent nova CI Aql (Hachisu & Kato 2003a), the Large Magellanic Cloud (LMC) SSS RX J0513.9-6951 (Hachisu & Kato 2003b), and V Sge (Hachisu & Kato 2003c).

Assuming an accretion disk whose edge is flaring up by the stream impact from the L1 point, Schandl et al. (1997) explained the orbital phase brightness variation of the supersoft X-ray sources in the LMC. We also assume that the disk edge is elevating up to 0.3 times the disk size, $\beta \leq 0.3$ in Equation (B2), after the winds stop, that is, in the SSS phase of KT Eri.

We adopt a disk whose size is 1.3 times the Roche-lobe radius of the WD, as shown in Figure 5a, during

the nova wind phase. The $\alpha = 1.3$ is taken from the observational result on the 2022 outburst of U Sco (see Figure 5 of Muraoka et al. 2024). After the nova winds stop, we assume the size of the disk to be 0.9 times the Roche-lobe radius of the WD, $\alpha = 0.9$ in Equation (B1), as shown in Figure 5b.

The photospheric mesh surfaces in Figure 5, i.e., of the disk and companion star, are irradiated by the central hot WD. Then, the photospheric temperatures increase and emit photons at these increased temperatures. Such irradiation effects are all included in the calculation of the V light curve reproduction (see Hachisu & Kato 2001, for the partition of each surface and calculation method of irradiation). Note that, in Figure 5, gas is optically thin outside the mesh surfaces (i.e., photospheres of the disk, WD, and companion star). In our irradiation calculation, we neglect absorption by optically thin gas outside the mesh surfaces.

B.4. Composite light curves: first plateau

We have calculated the composite light curves as follows. In an early phase of the outburst, free-free emission from the wind dominates the V band flux and the FF+BB model light curve well follows the V, y light curves until day ~ 40 . When the WD photosphere shrinks to $R_{\text{ph}} \sim 0.3 R_{\odot}$ ($\sim 0.08 R_{\text{RL},1}$), i.e., ~ 30 days after the outburst, the irradiated part of the disk had already emerged from the WD photosphere. The large disk begins to contribute to the V band luminosity comparably to the FF+BB flux.

We divide the surfaces of the WD, disk, and companion star into small segments as in Figure 5. Each patch of the WD emits photons as a blackbody of the temperature T_{ph} . Each patch of the disk and companion star absorbs photons from the WD, heats up, and then emits blackbody photons with a higher temperature than the original temperature. We calculate its V flux with a standard V filter response function and sum them up to obtain the total V flux. The calculation method is described in Hachisu & Kato (2001). Figure 8 depicts our model V light curves for such an irradiated disk (and companion star) as already described by Equation (5) in Figure 1b.

Our model well reproduces the brightness for the value of $\alpha = 1.3$ (and $\beta = 0.05$) during the wind phase. The thickness of $\beta = 0.05$ is not strictly constrained but is likely to be geometrically thin because its surface is blown in the wind.

The V, y brightnesses in the first plateau depends only on the size and shape of the disk and does not depend on the mass-accretion rate, \dot{M}_{acc} , or the photospheric temperature of the companion star, $T_{\text{ph},2}$, because the

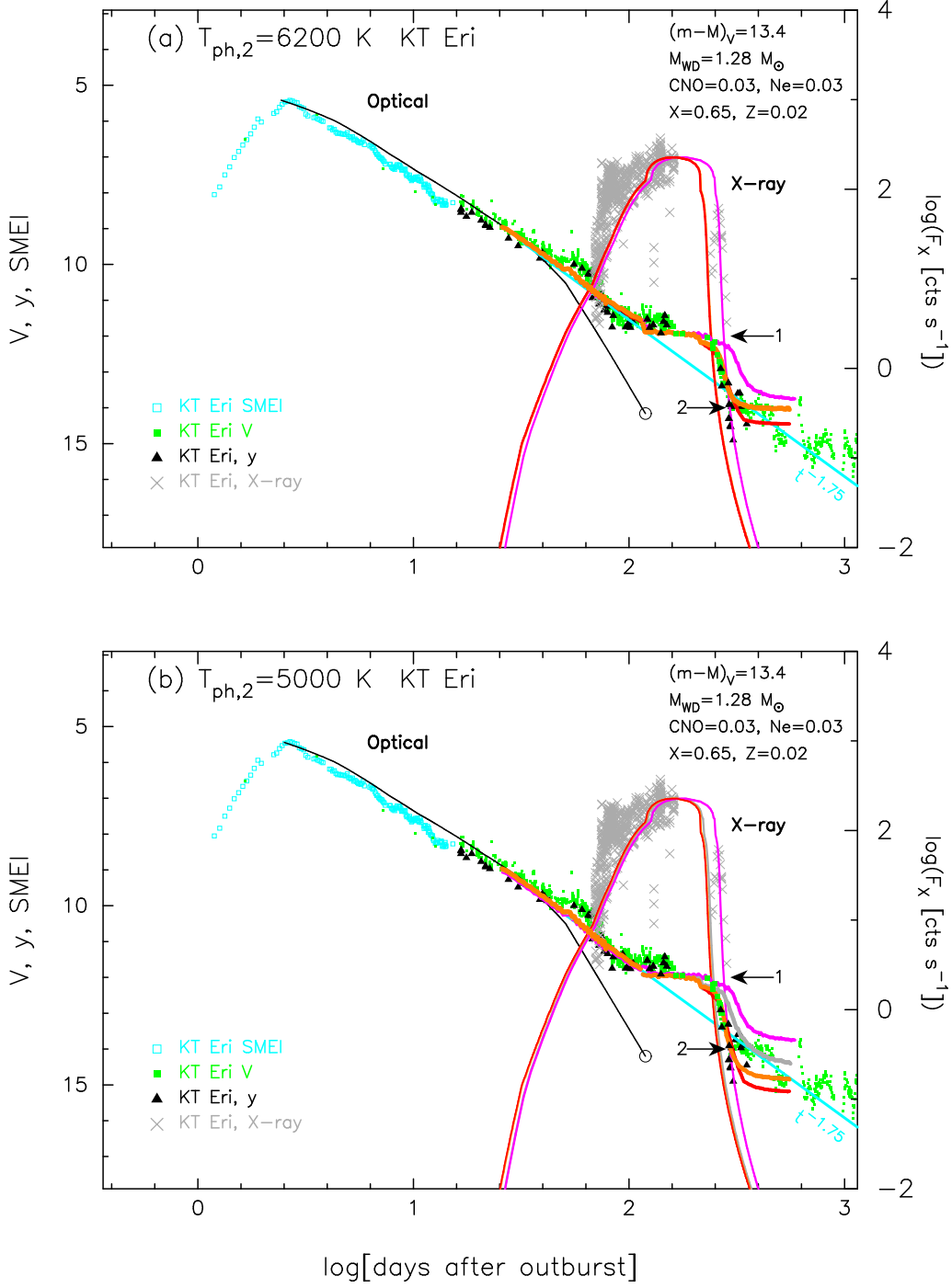


Figure 8. Same as Figure 1b, but for $M_{\text{WD}} = 1.28 M_{\odot}$ (Ne3). The parameters of each model are tabulated in Table 1. (a) We assume the photospheric temperature of the companion star to be $T_{\text{ph},2} = 6,200$ K (Schaefer et al. 2022). The black line depicts the FF+BB model light curve for KT Eri. The orange line reproduces both the first plateau (1: $V \sim 12.0$ mag) and the second plateau (2: $V \sim 14.1$ mag), in which the mass-accretion rate to the WD through the accretion disk is assumed to be $\dot{M}_{\text{acc}} = 1 \times 10^{-9} M_{\odot} \text{ yr}^{-1}$ and the disk shape parameters of $(\alpha, \beta) = (0.9, 0.01)$ in the second plateau. The magenta line denotes the case of $\dot{M}_{\text{acc}} = 1 \times 10^{-7} M_{\odot} \text{ yr}^{-1}$ and $(\alpha, \beta) = (0.9, 0.3)$, and the red line corresponds to $\dot{M}_{\text{acc}} = 1 \times 10^{-9} M_{\odot} \text{ yr}^{-1}$ and $(\alpha, \beta) = (0.3, 0.01)$. The corresponding X-ray light curves are plotted by the same color lines as those of model V light curves, but the orange and red lines are overlapped. (b) Same as those in panel (a) except $T_{\text{ph},2} = 5,000$ K. We added the gray line of $\dot{M}_{\text{acc}} = 3 \times 10^{-8} M_{\odot} \text{ yr}^{-1}$ and $(\alpha, \beta) = (0.9, 0.3)$.

Table 1. Parameters and brightnesses of the second plateau

M_{WD} (M_{\odot})	$T_{\text{ph},2}$ (K)	$-\dot{M}_2$ ($M_{\odot} \text{ yr}^{-1}$)	α	β	V^a (mag)	comment
1.28	6200	1×10^{-7}	0.9	0.3	13.7	8a,magenta ^b
1.28	6200	1×10^{-7}	0.9	0.01	13.7	
1.28	6200	1×10^{-8}	0.9	0.01	13.9	
1.28	6200	1×10^{-9}	0.9	0.01	14.0	8a,orange
1.28	6200	1×10^{-9}	0.9	0.1	13.9	
1.28	6200	1×10^{-9}	0.9	0.3	13.7	
1.28	6200	1×10^{-9}	0.3	0.01	14.4	8a,red
1.28	6200	1×10^{-9}	0.1	0.01	14.5	
1.28	6200	1×10^{-10}	0.9	0.01	14.0	
1.28	5000	1×10^{-7}	0.9	0.3	13.8	8b,magenta
1.28	5000	1×10^{-7}	0.9	0.01	14.4	
1.28	5000	3×10^{-8}	0.9	0.3	14.2	8b,gray
1.28	5000	1×10^{-8}	0.9	0.01	14.7	
1.28	5000	1×10^{-9}	0.9	0.01	14.8	8b,orange
1.28	5000	1×10^{-9}	0.9	0.1	14.6	
1.28	5000	1×10^{-9}	0.9	0.3	14.4	
1.28	5000	1×10^{-9}	0.3	0.01	15.2	8b,red
1.28	5000	1×10^{-9}	0.1	0.01	15.3	
1.28	5000	1×10^{-10}	0.9	0.01	14.8	
1.3	5000	2×10^{-7}	0.9	0.3	14.0	
1.3	5000	1×10^{-9}	0.9	0.01	14.8	
1.3	5000	1×10^{-9}	0.3	0.01	15.2	
1.3	5000	1×10^{-11}	0.01	0.01	15.3	
1.3	4500	2×10^{-7}	0.9	0.3	14.1	1b,magenta
1.3	4500	1×10^{-7}	0.9	0.01	14.6	1b,orange
1.3	4500	1×10^{-8}	0.9	0.01	15.1	
1.3	4500	1×10^{-9}	0.9	0.01	15.3	1b,red
1.3	4500	1×10^{-9}	0.3	0.01	15.6	
1.3	4500	1×10^{-11}	0.01	0.01	15.8	1b,gray

^a The model V magnitude at the second plateau for the distance modulus in the V band of $(m - M)_V = 13.4$. The inclination angle is $i = 40.9^\circ$ for $M_{\text{WD}} = 1.28 M_{\odot}$ (Ne3), the first 19 cases, but $i = 41.2^\circ$ for $M_{\text{WD}} = 1.3 M_{\odot}$ (Ne3), the last 10 models.

^b Magenta line in Figure 8a.

irradiation effect of the disk dominates the optical flux in the SSS phase. We need the size of the disk to be as large as $\alpha \gtrsim 0.9$ (for $\beta = 0.3$). If we reduce the height of the flaring edge down to $\beta = 0.1$, we do not reproduce the brightness of $V \sim 12.0$ in the first plateau. Thus, we adopt a flaring edge of $\beta = 0.3$.

B.5. Brightness in the second plateau

Unlike the first plateau, the V brightness in the second plateau depends on the mass-accretion rate. We calculate the V magnitudes with a combination of parameters $(\dot{M}_2, \alpha, \beta)$ for the second plateau. The results are listed in Table 1. Here, the mass transfer rate from the companion is equal to the mass accretion rate onto the WD, $\dot{M}_2 = -\dot{M}_{\text{WD}}$, under the mass conservation condition of $\dot{M}_{\text{WD}} + \dot{M}_2 = 0$. This means that, after the

nova winds stop, we neglect the effect of disk winds, L2 outflow, or winds from the companion star.

Assuming that the mass-losing rate of the companion star is $\dot{M}_2 = -1.0 \times 10^{-9} M_{\odot} \text{ yr}^{-1}$ and the disk shape of $(\alpha, \beta) = (0.9, 0.01)$ in the second plateau, we calculated the model V light curve (orange line in Figure 8a). The orange line reproduces the second plateau ($V \approx 14.0$). The brightness in the second plateau is also tabulated in Table 1. The effect of impact of the L1 stream becomes weak for such a low mass-transfer rate of $\dot{M}_2 = -1.0 \times 10^{-9} M_{\odot} \text{ yr}^{-1}$, so that we adopt a geometrically thin accretion disk ($\beta = 0.01$).

After the second plateau, the nova enters the quiescent phase and the V, y magnitudes go down to the quiescent level of $V \sim 15.1$. Our model (orange line) in Figure 8a, however, does not decay down to $V \sim 15.1$, but keep staying at $V \approx 14.0$. We changed the mass-losing rate \dot{M}_2 from -1×10^{-7} to $-1 \times 10^{-10} M_{\odot} \text{ yr}^{-1}$, but the brightness decreases only from $V = 13.7$ to 14.0 for $(\alpha, \beta) = (0.9, 0.01)$, as tabulated in Table 1.

Even if we change the size and shape of the disk, from $\alpha = 0.9$ to 0.1, from $\beta = 0.3$ to 0.01, the V magnitude varies between 13.7 and 14.5. We concluded that the photospheric temperature of the companion star, $T_{\text{ph},2} = 6,200$ K (Schaefer et al. 2022), is too high to be compatible with the observed V brightness in the quiescent phase ($V \sim 15.1 \pm 0.7$).

B.6. Brightness in quiescence

We have to reduce the photospheric temperature of the companion star from $T_{\text{ph},2} = 6,200$ K to $T_{\text{ph},2} = 5,000$ K, and calculate the brightness in the quiescent phase. The orange line in Figure 8b shows a model of $\dot{M}_2 = -1 \times 10^{-9} M_{\odot} \text{ yr}^{-1}$, $\alpha = 0.9$, and $\beta = 0.01$, which reproduces well the brightness of $V \sim 14.8$ in the quiescent phase.

However, we do not reproduce the lowest brightness of $V \sim 15.8$ by this $T_{\text{ph},2} = 5,000$ K model, as tabulated in Table 1. We must further decrease the photospheric temperature of the companion star down to $T_{\text{ph},2} = 4,500$ K. This will be examined in Section B.8.

B.7. Duration of the hydrogen burning

Figure 1a shows that the Swift X-ray count rate quickly dropped on day ~ 280 , and Figure 3b shows that the intensity of He II 4686Å line started to drop on day ~ 240 . We regard that these epochs correspond to the end of hydrogen burning. Figure 7 shows, however, that all of our best-fit optical models begin to decay earlier than the X-ray count rate does. Because we have already fixed two model parameters, i.e., the WD mass and chemical composition of the envelope, and the

X-ray turnoff time does not depend on the disk parameters, there remains one parameter, the mass-accretion rate to the WD, which could extend the period of hydrogen burning. We adopt four mass-accretion rates, $\dot{M}_{\text{acc}} = 1 \times 10^{-10}, 1 \times 10^{-9}, 1 \times 10^{-8},$ and $1 \times 10^{-7} M_{\odot} \text{ yr}^{-1}$, and examine how the mass-accretion rate changes the duration of hydrogen burning, i.e., the period of the SSS phase. Especially, high mass-accretion rates supply fuel effectively to hydrogen burning and make its duration significantly longer, as expected from Equation (4). These parameters are summarized in Table 1.

Among these four \dot{M}_{acc} models, the $\dot{M}_{\text{acc}} = 1 \times 10^{-7} M_{\odot} \text{ yr}^{-1}$ model catches up the X-ray decay on day ~ 280 , as indicated by the thin magenta lines in Figure 8a and b. On the other hand, this model (the thick magenta lines in both Figure 8a and b) does not correctly follow the optical V, y observation; the decay to the second plateau is too late.

In this way, we have examined $1.28 M_{\odot}$ WD (Ne3) models with various parameters, but there seem to be no models that satisfy all the observational requirements.

B.8. The $1.3 M_{\odot}$ WD (Ne3)

We finally adopt a $1.3 M_{\odot}$ WD (Ne3) for our KT Eri model. We first assume that $T_{\text{ph},2} = 5,000$ K for $M_2 = 1.0 M_{\odot}$. The model of $(-\dot{M}_2, \alpha, \beta) = (2 \times 10^{-7} M_{\odot} \text{ yr}^{-1}, 0.9, 0.3)$ reproduces both the first ($V \sim 12.1$) and second ($V \sim 14.0$) plateau including their temporal variations as well as their V brightnesses. This means that the mass-accretion rate and the size and shape of the disk are kept constant in the first and second plateaus until the second plateau ends.

The cases of $(-\dot{M}_2, \alpha, \beta) = (1 \times 10^{-9} M_{\odot} \text{ yr}^{-1}, 0.9, 0.01), (1 \times 10^{-9} M_{\odot} \text{ yr}^{-1}, 0.3, 0.01),$ and $(1 \times 10^{-11} M_{\odot} \text{ yr}^{-1}, 0.01, 0.01)$ show the brightness of $V \sim 14.8, 15.2,$ and 15.3 , respectively, in quiescence, as summarized in Table 1. Thus, the average brightness $V \sim 15.1$ in quiescence can be explained by this $M_{\text{WD}} = 1.3 M_{\odot}$ WD and $T_{\text{ph},2} = 5,000$ K model.

Therefore, we may conclude that the transition from the second plateau to the quiescence is driven by the reductions of the mass-transfer rate from $-\dot{M}_2 = 2 \times 10^{-7}$ to $1 \times 10^{-9} M_{\odot} \text{ yr}^{-1}$ and the flaring-up factor from $\beta = 0.3$ to 0.01 . This reminds us that high mass transfer rates such as $2 \times 10^{-7} M_{\odot} \text{ yr}^{-1}$ makes a spray at the edge of the disk as illustrated by Schandl et al. (1997).

The faintest brightness in quiescence, however, is as low as about $V \sim 15.8$ (Schaefer et al. 2022). This low brightness is obtained for $T_{\text{ph},2} = 4,500$ K, as shown by the gray line in Figure 1b and Table 1. In this case, the parameters are $(-\dot{M}_2, \alpha, \beta) = (1 \times 10^{-11} M_{\odot}$

$\text{ yr}^{-1}, 0.01, 0.01)$. This means that the WD and disk component are negligible. In other words, the mass-transfer virtually stops and then the disk almost disappears. If we could obtain spectral energy distribution of KT Eri in the faintest state, we would determine the nature of the companion star. Our estimate on the variable $-\dot{M}_2$ is consistent with Sun et al. (2020)'s low mass-accretion rate of $\dot{M}_{\text{acc}} \approx 1.9 \times 10^{-10} (d/3.7 \text{ kpc})^2 M_{\odot} \text{ yr}^{-1}$ about 8.3 yr after the outburst. The origin of such a variation in the mass-transfer rate is unclear.

Schaefer et al. (2022) obtained a very high mass-losing rate of $\dot{M}_2 = -3.5 \times 10^{-7} (d/5.1 \text{ kpc})^2 M_{\odot} \text{ yr}^{-1}$ as an average in quiescence. If this is the case, hydrogen burning never stops ($-\dot{M}_2 \gtrsim \dot{M}_{\text{steady}} \approx 3 \times 10^{-7} M_{\odot} \text{ yr}^{-1}$ for $M_{\text{WD}} = 1.3 M_{\odot}$), the SSS phase never ends, the V, y brightnesses keep $V, y \sim 12.0$ for a long time, and never drops to $V \sim 15$.

We may conclude that the average mass-transfer rate is as low as $\dot{M}_2 \sim -1 \times 10^{-9} M_{\odot} \text{ yr}^{-1}$ ($V \sim 15.3$ and $\dot{M}_{\text{WD}} \ll \dot{M}_{\text{steady}}$) before the outburst and increases to $-\dot{M}_2 \sim 2 \times 10^{-7} M_{\odot} \text{ yr}^{-1}$ when the winds stopped on day ~ 100 . It should be noted that, in this model, we can explain both the brightness in the second plateau and the SSS duration at the same time with a single mass accretion rate of $\dot{M}_{\text{acc}} = 2 \times 10^{-7} M_{\odot} \text{ yr}^{-1}$.

Finally, we have checked the case of $M_{\text{WD}} = 1.32 M_{\odot}$ (Ne3), because the three cases of $M_{\text{WD}} = 1.28, 1.3,$ and $1.32 M_{\odot}$ (Ne3) satisfy the observational constraints except for the decay of supersoft X-ray light curve in Figure 7b (see Appendix A). We adopt $\dot{M}_2 \sim -2 \times 10^{-7} M_{\odot} \text{ yr}^{-1}$ and $(\alpha, \beta) = (1.3, 0.05)$ in the wind phase, $(0.9, 0.3)$ in the SSS phase (the first plateau) and in the second plateau. The V brightness reproduces $V \sim 12.0$ in the first plateau and $V \sim 14.1$ in the second plateau but each start and end epochs are too early to be compatible with the observation. For example, the end epoch of hydrogen burning is day ~ 190 , about 50 days earlier. Thus, we may exclude the WD masses of $1.32 M_{\odot}$ and conclude that the WD mass is $1.28 M_{\odot} < M_{\text{WD}} < 1.32 M_{\odot}$.

C. DISTANCE MODULI IN THE $B, V,$ AND I_C BANDS

C.1. The time-stretching method

The distance to KT Eri is a little bit controversial between $d = 4.2$ kpc (Gaia eDR3, Schaefer 2022b, the present work) and $d = 5.1$ kpc (Schaefer et al. 2022), as introduced in Section 2.1. In this Appendix, we apply the time-stretching method to KT Eri and LV Vul, and obtain the distance to the nova (Hachisu & Kato 2010, 2015, 2016b).

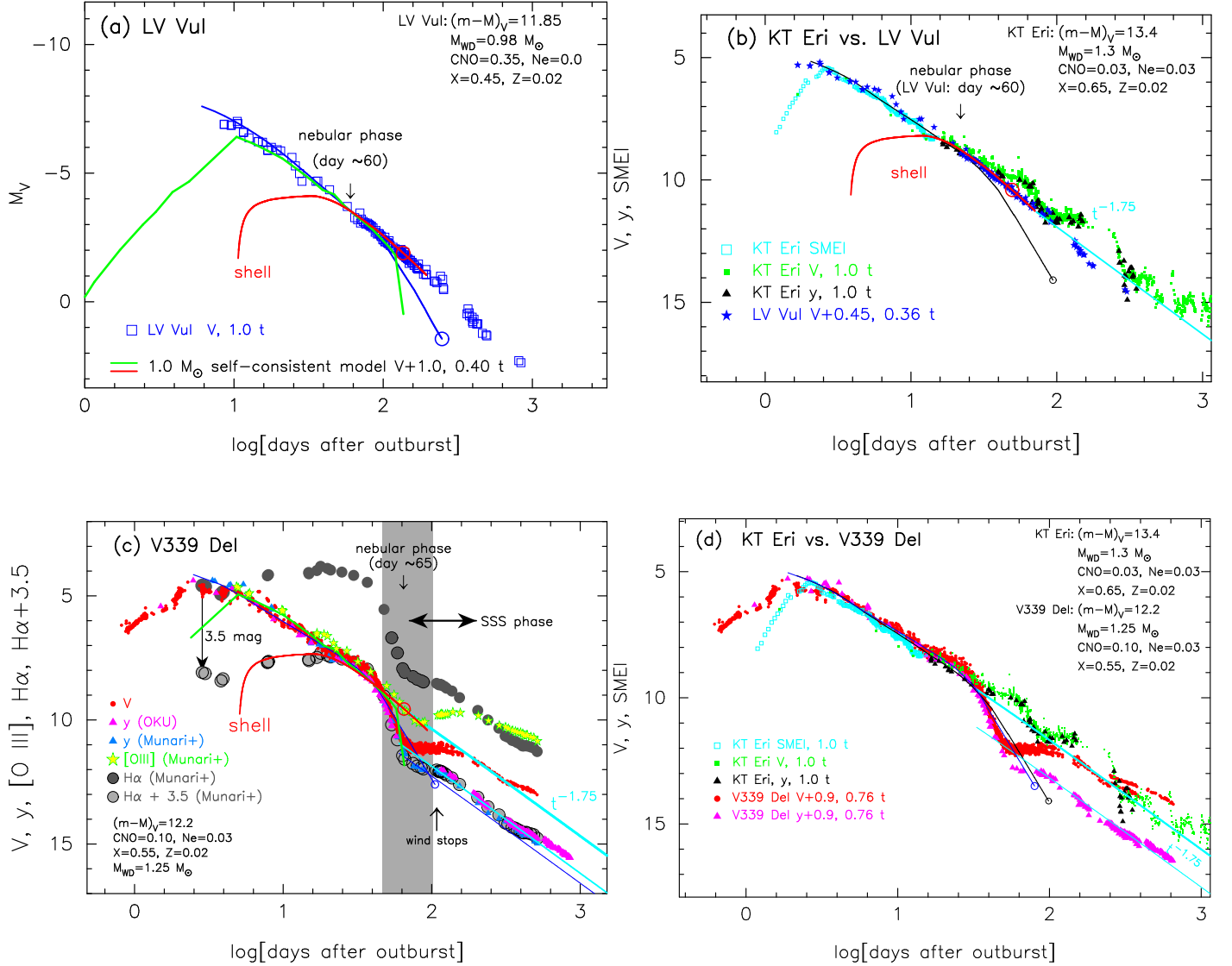


Figure 9. (a) The V light curve of the classical nova LV Vul for $(m - M)_V = 11.85$ (Hachisu & Kato 2021). The V data are the same as those in Hachisu & Kato (2016b). We indicate the start of the nebular phase of LV Vul about 60 days after the outburst (Hachisu & Kato 2016b). The blue line depicts a best-fit FF+BB model in Hachisu & Kato (2019), that is, a $0.98 M_{\odot}$ WD (CO3: $X = 0.45$, $Y = 0.18$, $Z = 0.02$, $X_{\text{CNO}} = 0.35$, $X_{\text{Ne}} = 0$) among Kato & Hachisu (1994)’s nova models. The green one denotes the free-free plus blackbody (FF+BB) flux (Kato et al. 2022a; Hachisu & Kato 2023) and the red one does the emission from the shocked shell based on the shock model of Hachisu & Kato (2022). The open red circle on the red line indicates the end epoch of winds (Hachisu & Kato 2023). These two lines are calculated from the time-stretched $1.0 M_{\odot}$ self-consistent nova outburst model (Hachisu & Kato 2023): $f_s = 0.4$ and $\Delta V = +1.0$ in Equation (C5) for target= LV Vul and template= $1.0 M_{\odot}$ WD model. (b) Comparison between KT Eri and LV Vul with $f_s = 0.36$ and $\Delta V = +0.45$. The black line denotes our FF+BB model light curve of a $1.3 M_{\odot}$ WD (Ne3) for KT Eri. We indicate the slope of $L_V \propto t^{-1.75}$ (the thick cyan line). (c) The V , y , [O III], H α , and H α + 3.5 mag light curves of the classical nova V339 Del. The data are the same as those in Figure 8(a) of Hachisu et al. (2024). The gray-shaded region represents the substantial absorption phase by a dust shell. We indicate the SSS phase by the two-headed arrow labeled “SSS phase.” The curved blue line is the FF+BB light curve of a $1.25 M_{\odot}$ WD (Ne2) model for V339 Del, which is taken from Hachisu et al. (2024). The green and red lines are the same as those in panel (a), but with $f_s = 0.145$ and $\Delta V = +1.45$. The H α + 3.5 mag light curve first follows the shape of the shell emission because the H α line comes from the shocked shell (Hachisu et al. 2024). (d) Comparison between KT Eri and V339 Del with the time-stretching factor of $f_s = 0.76$ and $\Delta V = +0.9$. The other symbols and lines are the same as those in panels (b) and (c).

This method is based on the similarity of nova light curves. Adopting appropriate time-stretching parameters, we are able to overlap two nova light curves even if the two nova speed classes are different. If the two nova V light curves, i.e., one is called the template and the other is called the target, $(m[t])_{V,\text{target}}$ and $(m[t])_{V,\text{template}}$ overlap each other after time-stretching of a factor of f_s in the horizontal direction and shifting vertically down by ΔV , i.e.,

$$(m[t])_{V,\text{target}} = ((m[t \times f_s])_V + \Delta V)_{\text{template}}, \quad (\text{C5})$$

their distance moduli in the V band satisfy

$$(m - M)_{V,\text{target}} = ((m - M)_V + \Delta V)_{\text{template}} - 2.5 \log f_s, \quad (\text{C6})$$

where m_V and M_V are the apparent and absolute V magnitudes, and $(m - M)_{V,\text{target}}$ and $(m - M)_{V,\text{template}}$ are the distance moduli in the V band of the target and template novae (e.g., Hachisu et al. 2020).

Figure 9a shows the V light curve of the classical nova LV Vul. Here, we time-stretch the light curves of Kato et al. (2022a)'s self-consistent nova model (green and red lines) against that of LV Vul (open blue squares) by the time-shift of $\Delta \log t = \log f_s = \log 0.4 = -0.4$ in the horizontal direction and the vertical shift by $\Delta V = +1.0$. The green line denotes the free-free plus blackbody (FF+BB) model light curve while the red line represents the shell emission of the self-consistent nova model, both of which were calculated by Hachisu & Kato (2023). The shell emission comes from the shocked shell far outside the nova photosphere (see Figure 6a and c). In Figure 9b, we further time-stretch the V light curve of LV Vul and overlap it with the V, y light curves of KT Eri. The time-stretching factor is $f_s = 0.36$, that is, the time-shift by $\Delta \log t = \log f_s = -0.44$ in the horizontal direction and the vertical shift by $\Delta V = +0.45$ mag. The V light curve (filled blue stars) declines almost along with the same universal decline law of $L_V \propto t^{-1.75}$ (thick cyan line) over the nebular phase.

Applying Equation (C6) to KT Eri and LV Vul in Figure 9b, we obtain

$$\begin{aligned} (m - M)_{V,\text{KT Eri}} &= ((m - M)_V + \Delta V)_{\text{LV Vul}} - 2.5 \log 0.36 \\ &= 11.85 + 0.45 \pm 0.2 + 1.1 = 13.4 \pm 0.2, \end{aligned} \quad (\text{C7})$$

where we adopt $(m - M)_{V,\text{LV Vul}} = 11.85$ from Hachisu & Kato (2021). Thus, we obtain $(m - M)_{V,\text{KT Eri}} = 13.4 \pm 0.2$, which is consistent with the Gaia eDR3 distance of $d = 4.1_{-0.4}^{+0.5}$ kpc (Bailer-Jones et al. 2021) and Schaefer (2022b)'s distance of $d = 4211_{-296}^{+466}$ pc together with the extinction

of $E(B - V) = 0.08$ (Ragan et al. 2009). The distance modulus in the V band of $(m - M)_{V,\text{KT Eri}} = 13.4 \pm 0.2$ is also supported by our $1.3 M_\odot$ WD model in Figure 1b.

C.2. Universal decline law in the nebular phase

Many novae show the universal decline law of $L_V \propto t^{-1.75}$ even in the nebular phase (Hachisu & Kato 2006, 2010, 2023). On the other hand, the FF+BB model light curves follow the universal decline law until the start of the nebular phase but, after that, depart from the V light curve (see, e.g., Figure 9a for LV Vul). We discuss this issue for LV Vul and KT Eri based on the results of Hachisu & Kato (2023). The FF+BB light curve of the self-consistent nova model (green line in Figure 9a) reaches its maximum light and then declines almost along the universal decline law of $L_V \propto t^{-1.75}$. It rapidly decreases just before optically thick winds stop (at the open red circle on the red line in Figure 9a). This is because the free-free flux depends on the square of wind mass-loss rate, i.e., $L_{V,\text{ff,wind}} \propto \dot{M}_{\text{wind}}^2$ from Equation (2), and \dot{M}_{wind} is rapidly decreasing just before winds stop.

Then, the density of winds is also rapidly decreasing and the photospheric temperature increases (see, e.g., Figure 5 of Hachisu et al. 2024, for the temporal variation of the photospheric temperature). Both the quick decrease in the wind density and the rapid increase in the temperature of the radiation field are suitable for the excitation of [O III] 4959, 5007Å lines. Hachisu et al. (2024) analyzed the temporal flux variation of [O III] lines for V339 Del (Figure 9c) and found that the [O III] emission lines comes from the shocked shell. Arai et al. (2013) analyzed [O III] 4959, 5007Å lines of KT Eri obtained on day 294 (in the nebular phase). Their decomposed doublet [O III] line profiles show a broad 2,200 km s⁻¹ rectangular (pedestal) shape in the second plot of their Figure 2. This is consistent with our interpretation that [O III] 4959, 5007Å lines come from the shocked shell as illustrated in Figure 6c.

The shell emission of the self-consistent nova model (red line in Figure 9a) is calculated from the flux from the shocked shell (see Figure 6a and c) and eventually dominates the V luminosity in the nebular phase. See Equation (B6) of Hachisu & Kato (2023) for the calculation of the red line. In this LV Vul case in Figure 9a, the shell emission in the V band is dominated by [O III] lines. The fluxes of [O III] 4959, 5007Å lines follows the same universal decline law of $L_V \propto t^{-1.75}$ in the nebular phase. Thus, the shell emission takes over the FF+BB flux and extends our universal decline law

of $L_V \propto t^{-1.75}$ even to the nebular phase (the red line in Figure 9b).

To summarize, the FF+BB flux decays rapidly after the nebular phase started. The flux of strong [O III] emission lines increases and fills the gap between the FF+BB flux and the V observation. This is the reason why many novae follow the universal decline law even in the nebular phase.

If the dominant source in the V band is [O III] 4959, 5007Å lines, the V magnitude should be much brighter than the y magnitude in the nebular phase, because the y band filter is designed to avoid the [O III] 4959, 5007Å lines. Such examples are V1500 Cyg, V1668 Cyg, and V339 Del, as already introduced in Section 2.4.

We may conclude that the nebular phase of a nova is driven by (1) the quick decrease in the wind mass-loss rate \dot{M}_{wind} and (2) the concurrent rapid rise of the photospheric temperature of a nova T_{ph} , both of which are inherent properties of a nova outburst. We add (3) that [O III] 4959, 5007Å lines are mainly excited in the shocked shell, which is far outside the photosphere. This is because the shocked shell eventually collects about 90% of the ejected mass (Hachisu & Kato 2022). Therefore, the line profiles of [O III] 4959, 5007Å are basically rectangles (or pedestals) if the shocked shell is spherically symmetric.

C.3. Comparison with V339 Del

Figure 9c depicts the light curves of the classical nova V339 Del in various bands (taken from Figure 8(a) of Hachisu et al. 2024), and Figure 9d displays the light curves both of V339 Del and KT Eri. V339 Del is a classical nova having a similar decay timescale to KT Eri. V339 Del also has a flat plateau in the V light curve during the SSS phase (e.g., Figure 1 of Shore et al. 2016) as denoted by the two-headed arrow labeled “SSS phase” in Figure 9c. The y magnitudes were well obtained from the optical peak to the very late phase of the outburst (Munari et al. 2015; Hachisu et al. 2024), as shown in Figure 9c and d. Unlike KT Eri, V339 Del shows a different property between the V and y magnitudes: the V light curve shows a flat plateau, but the y light curve does not. In this subsection, we deeply compare V339 Del with KT Eri and clarify the physical nature of the plateau phase in KT Eri.

Figure 9c shows five light curves of V , y , [O III], $H\alpha$, and $H\alpha + 3.5$ magnitudes of V339 Del. The V and y light curves decline very similarly until the nebular phase started on day ~ 65 (Munari et al. 2013c). After day ~ 65 , the y magnitude decline along the thin blue line of $L_y \propto t^{-1.75}$, whereas the V magnitude levels off for a while between day ~ 65 and day ~ 140 ,

showing a flat plateau phase, and then declines along the thick cyan line of $L_V \propto t^{-1.75}$.

Hachisu et al. (2024) presented a detailed light curve model of V339 Del and clarified these complicated behavior. The FF+BB light curve (Equation (3)) of a $1.25 M_{\odot}$ WD (Ne2) broadly reproduced the V, y light curve until day ~ 50 . The $H\alpha + 3.5$ magnitude follows the emission from the shocked shell in the early phase (until day ~ 45). Thus, the $H\alpha$ is shock-origin, at least, in an early phase of V339 Del. After day ~ 45 , both the V and y light curve drastically drop along the FF+BB light curve because the model wind mass-loss rate quickly drops and the model free-free flux from the nova wind sharply drops ($L_{V,\text{ff,wind}} \propto \dot{M}_{\text{wind}}^2$ from Equation (2), Hachisu & Kato 2006). A part of the V, y fluxes are absorbed by dust (Hachisu et al. 2024). After day ~ 65 , the y light curve is monotonically declining with the slope of $L_y \propto t^{-1.75}$ (thin blue or cyan line), which means the continuum emission declines as $L_y \propto t^{-1.75}$. On the other hand, the V light curve levels off and keeps a flat plateau of $V \sim 11$ between day ~ 65 and day ~ 140 , and then starts to decline with the same slope of $L_V \propto t^{-1.75}$ (thick cyan line). Thus, the V magnitude is about 1.5 mag brighter than the y magnitude after day ~ 140 . The [O III] emission line fluxes contribute to the V band flux and fills the gap between V and y (Munari et al. 2015).

A dust shell could be formed within a cool and dense shell behind the radiative shock in a nova ejecta (e.g., Derdzinski et al. 2017). The [O III] emission line originates from the layer slightly outside the dust shell in the shocked shell, because the [O III] light curve does not show a dust dip between day ~ 45 and day ~ 140 in Figure 9c. This means that each layer is ordered, the shock, dust, and [O III] emission, from inside to outside. Hachisu et al. (2024) concluded that the [O III] emission line comes from the outermost layer of the shocked shell. The $H\alpha$ (+3.5 mag), which shows a rapid decay after day ~ 45 compared with the shell emission light curve (red line), resides at the shock and dust, so that it could be suppressed and absorbed by dust (and cool environment). In this way, the difference among V , y , and [O III] tells us how the shocked shell contributes to the luminosity.

The V light curve of V339 Del shows a plateau during its SSS phase (from day ~ 72 to day ~ 200) while the y light curve does not (Figure 9c). The plateau of V339 Del in the V light curve is caused by the increase in the [O III] line emission, therefore, it does not mean an irradiation effect of the disk. Moreover, V339 Del is a close binary having a short orbital period of $P_{\text{orb}} = 0.163$ days (Schaefer 2022a). Thus, it cannot have a large accre-

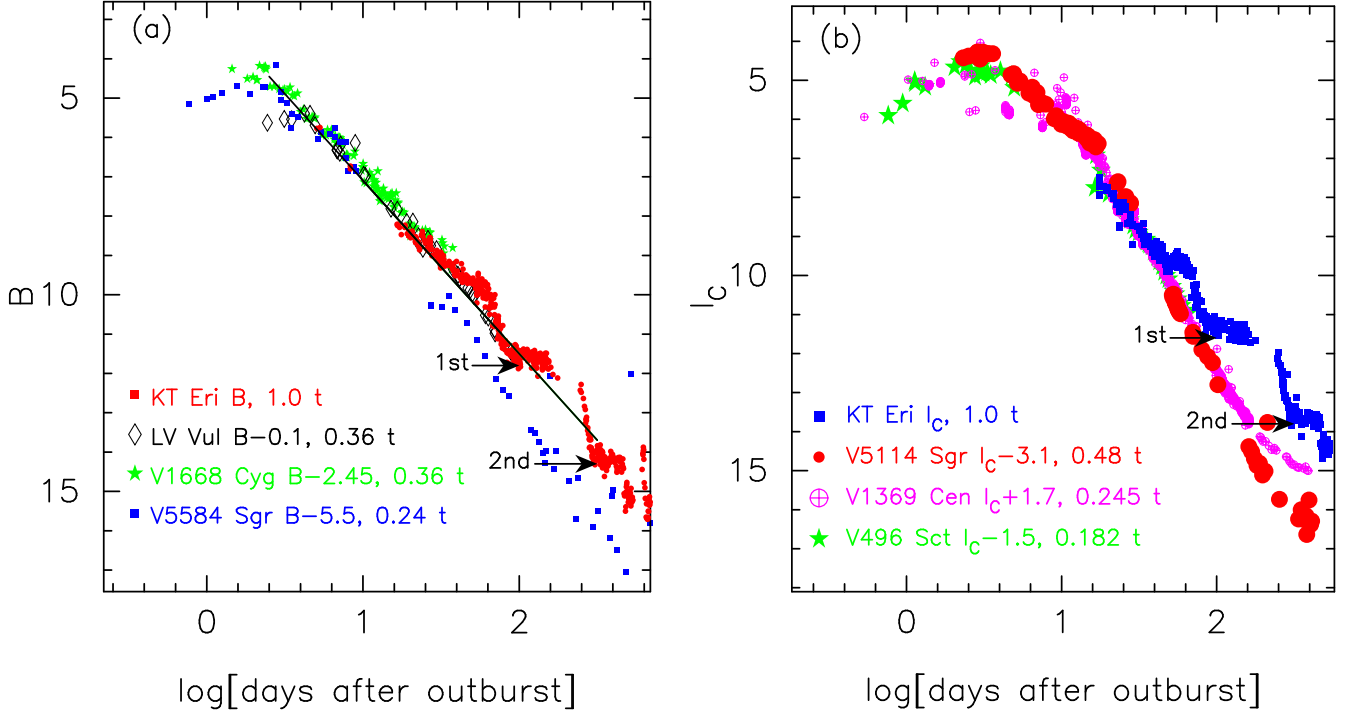


Figure 10. (a) The B light curve of KT Eri as well as those of LV Vul, V1668 Cyg, and V5584 Sgr. The B data of KT Eri are taken from VSOLJ, AAVSO, SMARTS, and [Imamura & Tanabe \(2012\)](#). The B data of the other novae are the same as those in [Hachisu & Kato \(2019, 2021\)](#). Each light curve is horizontally moved by $\Delta \log t = \log f_s$ and vertically shifted by ΔB with respect to that of KT Eri, as indicated by “LV Vul $B = -0.1, 0.36 t$,” which means $\Delta B = -0.05$ and $\Delta \log t = \log f_s = \log 0.36 = -0.44$. The solid black line denotes the slope of $L_B \propto t^{-1.75}$, where L_B is the B band luminosity. This slope is the trend of the universal decline law ([Hachisu & Kato 2006](#)). Horizontal arrows indicate the “1st” and “2nd” plateaus corresponding to the first and second plateaus in the V, y magnitudes of KT Eri. (b) Same as panel (a), but for the I_C light curve. The I_C data of KT Eri are taken from VSOLJ, AAVSO, and SMARTS. We add the I_C light curves of V5114 Sgr, V1369 Cen, and V496 Sct. The I_C data of the other novae are the same as those in [Hachisu & Kato \(2021\)](#).

tion disk like KT Eri. From such an example, we would stress that only a V flat plateau does not guarantee the presence of a bright disk during a supersoft X-ray source phase.

Figure 9d shows the V and y light curves both for KT Eri and V339 Del. The bright plateau of KT Eri is always above the thick cyan line of $L_V \propto t^{-1.75}$ (universal decline law: [Hachisu & Kato 2006](#)) while the plateau of V339 Del is below this thick cyan line. This simply means that the shell emission in the V band (typically [O III] lines in the nebular phase) is fainter than the bright large disk in KT Eri. We can see this in Figure 3a, where the flux of continuum is larger than that of [O III] lines. [Arai et al. \(2013\)](#) decomposed the doublet [O III] 4959, 5007Å lines of KT Eri on day 294 (=UT 2010 September 1) and showed that each component has a broad rectangular shape (shocked shell) with an expansion velocity of about $\sim 2,200 \text{ km s}^{-1}$ (second plot from the top in Figure 2 of [Arai et al. 2013](#)). As shown in Figure 6b in Section 3.2.1 and Figure 6d in Section

3.2.2, pedestal (rectangular shape) emission line profiles are an indication of a spherical shell. This confirms our interpretation that the [O III] lines are originated from the shocked shell.

In Figure 9d, the light curves of V339 Del are time-stretched with $f_s = 0.76$ and $\Delta V = +0.9$ against those of KT Eri. The distance modulus in the V band is obtained to be

$$\begin{aligned} (m - M)_{V, \text{KT Eri}} &= ((m - M)_V + \Delta V)_{\text{V339 Del}} - 2.5 \log 0.76 \\ &= 12.2 + 0.9 \pm 0.2 + 0.3 = 13.4 \pm 0.2, \end{aligned} \quad (\text{C8})$$

where we adopt $(m - M)_{V, \text{V339 Del}} = 12.2$ from [Hachisu et al. \(2024\)](#). Thus, we again obtain $(m - M)_V = 13.4 \pm 0.2$ for KT Eri.

Finally, we would like to stress that y magnitude observations are critically important for novae in order to identify whether or not a plateau phase is caused by a bright accretion disk. However, there are only a few novae that have been well followed with y magnitude.

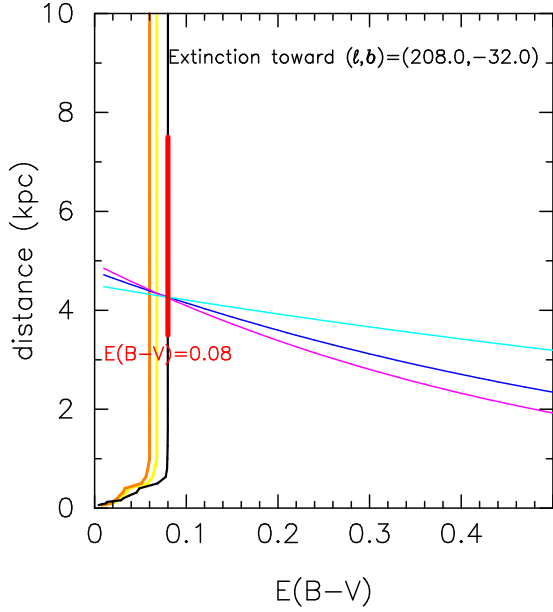


Figure 11. Various distance-reddening relations toward KT Eri. The three thin lines of magenta, blue, and cyan denote the distance-reddening relations given by $(m - M)_B = 13.47$, $(m - M)_V = 13.4$, and $(m - M)_I = 13.27$, respectively. These three lines cross broadly at $d = 4.2$ kpc and $E(B - V) = 0.08$ (thick vertical red line). Three thick black, orange, and yellow lines indicate the galactic distance-reddening relation toward the direction of KT Eri given by Green et al. (2015), Green et al. (2018), and Green et al. (2019), respectively.

The difference/similarity in the V, y light curves provide important information on the nova outburst and binary nature.

C.4. Time-stretching method in the B and I_C bands

We apply the time-stretching method to the B and I_C light curves of KT Eri and obtain the distance moduli both in the B and I_C bands. Figure 10a shows the B light curves of KT Eri together with those of LV Vul, V1668 Cyg, and V5584 Sgr. We apply Equation (C6) in the B band to Figure 10a and obtain

$$\begin{aligned}
 (m - M)_{B, \text{KT Eri}} &= ((m - M)_B + \Delta B)_{\text{LV Vul}} - 2.5 \log 0.36 \\
 &= 12.45 - 0.1 \pm 0.2 + 1.1 = 13.45 \pm 0.2 \\
 &= ((m - M)_B + \Delta B)_{\text{V1668 Cyg}} - 2.5 \log 0.36 \\
 &= 14.9 - 2.45 \pm 0.2 + 1.1 = 13.45 \pm 0.2 \\
 &= ((m - M)_B + \Delta B)_{\text{V5584 Sgr}} - 2.5 \log 0.24 \\
 &= 17.45 - 5.5 \pm 0.2 + 1.55 = 13.5 \pm 0.2, \quad (\text{C9})
 \end{aligned}$$

where we adopt the same stretching factor of $f_s = 0.36$ for LV Vul as in Figure 9b, and $(m - M)_{B, \text{LV Vul}} = 12.45$, $(m - M)_{B, \text{V1668 Cyg}} = 14.9$ and $f_s = 0.36$, $(m - M)_{B, \text{V5584 Sgr}} = 16.7 + 0.75 = 17.45$ and $f_s = 0.24$,

all taken from Hachisu & Kato (2021). Thus, we have $(m - M)_{B, \text{KT Eri}} = 13.47 \pm 0.2$.

Figure 10b shows the I_C light curve of KT Eri together with those of V5114 Sgr, V1369 Cen, and V496 Sct. These four I_C light curves broadly overlap with each other, although the I_C light curve of KT Eri is located slightly above the other three light curves in the later phase. This is because an irradiation effect of a large disk contributes to the luminosity in the I_C band. Applying Equation (C6) in the I_C band to Figure 10b, we obtain

$$\begin{aligned}
 (m - M)_{I, \text{KT Eri}} &= ((m - M)_I + \Delta I_C)_{\text{V5114 Sgr}} - 2.5 \log 0.48 \\
 &= 15.56 - 3.1 \pm 0.2 + 0.8 = 13.26 \pm 0.2 \\
 &= ((m - M)_I + \Delta I_C)_{\text{V1369 Cen}} - 2.5 \log 0.245 \\
 &= 10.1 + 1.7 \pm 0.2 + 1.52 = 13.32 \pm 0.2 \\
 &= ((m - M)_I + \Delta I_C)_{\text{V496 Sct}} - 2.5 \log 0.182 \\
 &= 12.9 - 1.5 \pm 0.2 + 1.85 = 13.25 \pm 0.2, \quad (\text{C10})
 \end{aligned}$$

where we adopt $(m - M)_{I, \text{V5114 Sgr}} = 15.56$ and $f_s = 0.48$ against that of KT Eri, $(m - M)_{I, \text{V1369 Cen}} = 10.1$ and $f_s = 0.245$, and $(m - M)_{I, \text{V496 Sct}} = 12.9$ and $f_s = 0.182$, all taken from Hachisu & Kato (2021). We obtain $(m - M)_{I, \text{KT Eri}} = 13.27 \pm 0.2$

We plot the distance-reddening relations in these three B , V , and I_C bands in Figure 11 by the magenta, blue, and cyan lines, that is, $(m - M)_B = 13.47$, $(m - M)_V = 13.4$, and $(m - M)_I = 13.27$ together with Equation (1) and

$$(m - M)_B = 5 \log(d/10 \text{ pc}) + 4.1E(B - V), \quad (\text{C11})$$

and

$$(m - M)_I = 5 \log(d/10 \text{ pc}) + 1.5E(B - V), \quad (\text{C12})$$

where each coefficient of $E(B - V)$ is taken from Rieke & Lebofsky (1985). These three lines cross broadly at $d = 4.2$ kpc and $E(B - V) = 0.08$. The reddening of $E(B - V) = 0.08$ is consistent with that of Ragan et al. (2009).

C.5. Color-magnitude diagram and start of nebular phase

When the B and V light curves of the target nova overlap with the B and V light curves of the template nova, respectively, with the same time-stretching method, i.e., with the same time-stretching factor of f_s , the intrinsic $(B - V)_0$ color curve of the target nova also overlaps with the intrinsic $(B - V)_0$ color curve of the template nova. This implies that the time-stretched $(B - V)_0 - (M_V - 2.5 \log f_s)$ color-magnitude diagrams of the target and template novae overlap with each other (Hachisu & Kato 2019).

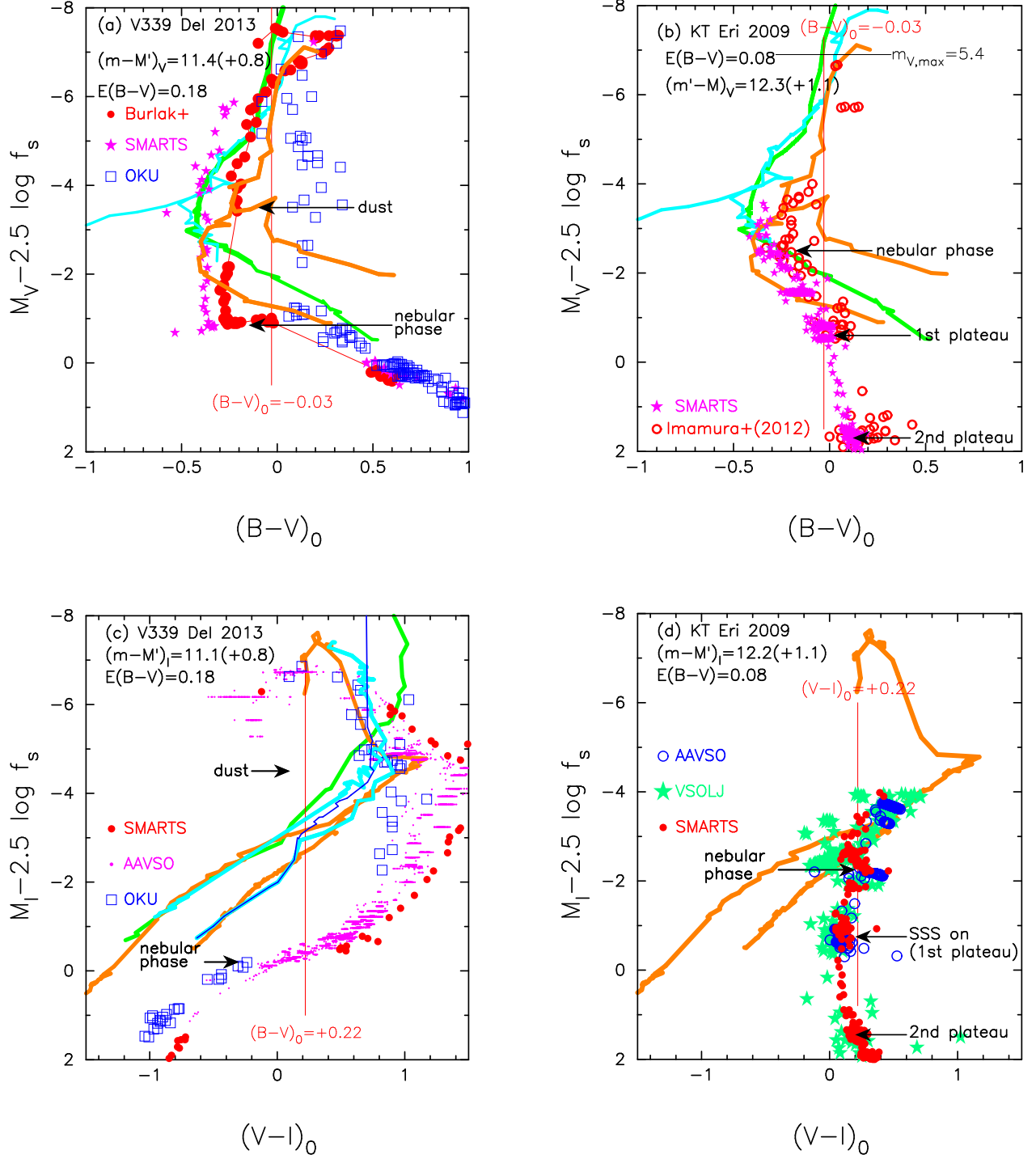


Figure 12. (a) The time-stretched $(B-V)_0$ - $(M_V - 2.5 \log f_s)$ color-magnitude diagram for V339 Del. The data of V339 Del are taken from Burlak et al. (2015), SMARTS (Walter et al. 2012), and OKU (Hachisu et al. 2024). The epochs of dust shell formation and start of the nebular phase are indicated by arrows. The vertical solid red line of $(B-V)_0 = -0.03$ is the intrinsic color of optically thick free-free emission (Hachisu & Kato 2014). The solid green, cyan, and orange lines denote the template tracks of V1500 Cyg, V1974 Cyg, and LV Vul, respectively. The track of V1974 Cyg/LV Vul splits into two branches in the later phase. See Hachisu & Kato (2016b) and Hachisu & Kato (2019) for details of these template tracks. (b) Same as in panel (a), but for KT Eri. The data of KT Eri are taken from SMARTS (Walter et al. 2012) and Imamura & Tanabe (2012). We specify the onset of nebular phase by a turning point of $(B-V)_0$ color, though not a usual definition. (c) The time-stretched $(V-I)_0$ - $(M_I - 2.5 \log f_s)$ color-magnitude diagram for V339 Del. The data of V339 Del are taken from AAVSO, SMARTS (Walter et al. 2012), and OKU (Hachisu et al. 2024). The thick solid lines of orange, green, blue, and cyan correspond to the outburst tracks of LV Vul, V1500 Cyg, V382 Vel, and LV Vul (V496 Sct, V959 Mon), which are taken from Hachisu & Kato (2021). (d) Same as those in panel (c), but for KT Eri.

Figure 12a shows the $(B - V)_0 - (M_V - 2.5 \log f_s)$ diagram for V339 Del while Figure 12b is for KT Eri. In the figures, we adopt $f_s = 0.48$ for V339 Del and $f_s = 0.36$ for KT Eri both against LV Vul, and the text of “ $(m - M')_V = 11.4(+0.8)$ ” in Figure 12a means the time-stretching distance modulus in the V band, that is, $(m - M')_V \equiv (m - M)_V - 2.5 \log f_s = 11.4$ and $(+0.8) \equiv -2.5 \log f_s = -2.5 \log 0.48 = +0.8$ for V339 Del. Then, the distance modulus in the V band is $(m - M)_V = 11.4 + 0.8 = 12.2$. The data of V339 Del are taken from Hachisu et al. (2024) while the data of KT Eri are from SMARTS (Walter et al. 2012) and Imamura & Tanabe (2012). We also plot the time-stretched color-magnitude diagrams for LV Vul (orange line), V1500 Cyg (green line), and V1974 Cyg (cyan line). All the data of these novae are the same as those in Hachisu & Kato (2019).

The color-magnitude tracks frequently show splitting into two or three (even more) branches depending on the observers (or telescopes). This is because the response function of each filter is slightly different among the telescopes and, as a result, strong emission lines at/near the blue or red edges of the filters contribute differently to the B and V band fluxes (see, e.g., Figure 1 of Munari et al. 2013a, for response functions).

Hachisu & Kato (2016b) extensively discussed the color-magnitude diagrams of many novae and concluded that a turning point/cusp of the track frequently corresponds to the onset of nebular phase. In V339 Del, dust shell formation influenced the color-magnitude track, but its turning point of the track, from toward blue to toward red, corresponds to the onset of the nebular phase as shown by the arrow labeled “nebular phase” in Figure 12a, which is detected with $[\text{O III}]/\text{H}\beta > 1$ by Munari et al. (2013c). The three tracks (Burlak+,

SMARTS, and Osaka Kyoiku University(OKU)) of V339 Del show a similar path in the very early phase, but split into three among the three observatories, and then merge into almost one path again in the very late phase. Thus, the nebular phase began at the turning points of these three tracks.

The two tracks of KT Eri (SMARTS and Imamura+) do not show a large split, because there are no stronger emission lines than the continuum and each emission line cannot contribute significantly to the B and V band fluxes (as already discussed in Section 2.4). The bright disk contributes both to the continuum flux and permitted emission lines such as $\text{H}\alpha$ and $\text{H}\beta$, which cloud the detection of nebular phase. In the present paper, we use a turning point of $(B - V)_0$ as the onset of nebular phase (as indicated by the arrow labeled “nebular phase” in Figure 12b). This turning point of $(B - V)_0$ corresponds to day ~ 40 , as already mentioned in Section 2.4.

There is a large difference between V339 Del and KT Eri: the trend of $(B - V)_0$ color in the later phase of V339 Del is toward red like the other classical novae (LV Vul, V1500 Cyg, and V1974 Cyg), but that of KT Eri seems to stay at/around $(B - V)_0 \sim 0.0$ in the first plateau and $(B - V)_0 \sim 0.2$ in the second plateau. The color of $(B - V)_0 \sim 0.0$ is a typical one for irradiated accretion disks as frequently observed in recurrent novae like in U Sco (see Figure 29(d) of Hachisu & Kato 2021).

We also plot the $(V - I)_0 - (M_I - 2.5 \log f_s)$ diagram for V339 Del and KT Eri in Figure 12c and 12d, respectively. Here, I corresponds to I_C . The $(V - I)_0$ color of KT Eri is close to 0.0-0.2 in the later phase of the outburst because the disk dominates the optical flux of KT Eri. The details of each tracks of the other novae are discussed in Hachisu & Kato (2021).

REFERENCES

- Arai, A., Isogai, M., Imamura, K., et al. Binary Paths to Type Ia Supernovae Explosions, Proceedings of the International Astronomical Union, IAU Symposium, Volume 281, p. 119-120, <https://doi.org/10.1017/S1743921312014809>
- Bailer-Jones, C. A. L., Rybizki, J., Fouesneau, M., Demleitner, M., & Andrae, R. 2021, AJ, 161, 147, <https://doi.org/10.3847/1538-3881/abd806>
- Bath, G. T. 1978, MNRAS, 182, 35, <https://doi.org/10.1093/mnras/182.1.35>
- Beals, C. S. 1931, MNRAS, 91, 966, <https://doi.org/10.1093/mnras/91.9.966>
- Beardmore, A. P., Balman, S., Osborne, J. P., et al. 2010, ATel, 2423, 1
- Bode, M. F., Osborne, J. P., Page, K. L., et al. 2010, ATel, 2392, 1
- Burlak, M. A., Esipov, V. F., Komissarova, G. V., et al. 2015, Baltic Astronomy, 24, 109, <https://doi.org/10.1515/astro-2017-0209>
- Cowley, A. P., Schmidtke, P. C., Crampton, D., Hutchings, J. B. 1998, ApJ, 504, 854, <https://doi.org/10.1086/306123>
- Darnley, M. J., Ribeiro, V. A. R. M., Bode, M. F., Hounsell, R. A., & Williams, R. P. 2012, ApJ, 746, 61, <https://doi.org/10.1088/0004-637X/746/1/61>

- della Valle, M., & Izzo, L. 2020, *The Astronomy and Astrophysics Review*, 28, 3,
<https://doi.org/10.1007/s00159-020-0124-6>
- Derdzinski, A. M., Metzger, B. D., & Lazzati, D. 2017, *MNRAS*, 469, 1314,
<https://doi.org/10.1093/mnras/stx829>
- Downes, R. A., & Duerbeck, H. W. 2000, *AJ*, 120, 2007,
<https://doi.org/10.1086/301551>
- Drake, J. J., & Orlando, S. 2010, *ApJL*, 720, L195,
<https://doi.org/10.1088/2041-8205/720/2/L195>
- Eggleton, P. P. 1983, *ApJ*, 268, 368,
<https://doi.org/10.1086/160960>
- Ennis, D., Becklin, E. E., Beckwith, S., et al. 1977, *ApJ*, 214, 478, <https://doi.org/10.1086/155273>
- Evans, P. A., Beardmore, A. P., Page, K. L., et al. 2009, *MNRAS*, 397, 1177,
<https://doi.org/10.1111/j.1365-2966.2009.14913.x>
- Gallagher, J. S., Kaler, J. B., Olson, E. C., Hartkopf, W. I., & Hunter, D. A. 1980, *PASP*, 92, 46,
<https://doi.org/10.1086/130612>
- Gallagher, J. S., & Ney, E. P. 1976, *ApJ*, 204, L35,
<https://doi.org/10.1086/182049>
- Green, G. M., Schlafly, E. F., Finkbeiner, D. P., et al. 2015, *ApJ*, 810, 25,
<https://doi.org/10.1088/0004-637X/810/1/25>
- Green, G. M., Schlafly, E. F., Finkbeiner, D. P., et al. 2018, *MNRAS*, 478, 651,
<https://doi.org/10.1093/mnras/sty1008>
- Green, G. M., Schlafly, E. F., Zucker, C., et al. 2019, *ApJ*, 887, 93 <https://doi.org/10.3847/1538-4357/ab5362>
- Hachisu, I., & Kato, M. 2001, *ApJ*, 558, 323,
<https://doi.org/10.1086/321601>
- Hachisu, I., & Kato, M. 2003a, *ApJ*, 588, 1003,
<https://doi.org/10.1086/374303>
- Hachisu, I., & Kato, M. 2003b, *ApJ*, 590, 445,
<https://doi.org/10.1086/374968>
- Hachisu, I., & Kato, M. 2003c, *ApJ*, 598, 527,
<https://doi.org/10.1086/378848>
- Hachisu, I., & Kato, M. 2006, *ApJS*, 167, 59,
<https://doi.org/10.1086/508063>
- Hachisu, I., & Kato, M. 2010, *ApJ*, 709, 680,
<https://doi.org/10.1088/0004-637X/709/2/680>
- Hachisu, I., & Kato, M. 2014, *ApJ*, 785, 97,
<https://doi.org/10.1088/0004-637X/785/2/97>
- Hachisu, I., & Kato, M. 2015, *ApJ*, 798, 76,
<https://doi.org/10.1088/0004-637X/798/2/76>
- Hachisu, I., & Kato, M. 2016a, *ApJ*, 816, 26,
<https://doi.org/10.3847/0004-637X/816/1/26>
- Hachisu, I., & Kato, M. 2016b, *ApJS*, 223, 21,
<https://doi.org/10.3847/0067-0049/223/2/21>
- Hachisu, I., & Kato, M. 2018, *ApJS*, 237, 4,
<https://doi.org/10.3847/1538-4365/aac833>
- Hachisu, I., & Kato, M. 2019, *ApJS*, 241, 4,
<https://doi.org/10.3847/1538-4365/ab0202>
- Hachisu, I., & Kato, M. 2021, *ApJS*, 253, 27,
<https://doi.org/10.3847/1538-4365/abd31e>
- Hachisu, I., & Kato, M. 2022, *ApJ*, 939, 1,
<https://doi.org/10.3847/1538-4357/ac9475>
- Hachisu, I., & Kato, M. 2023, *ApJ*, 953, 78,
<https://doi.org/10.3847/1538-4357/acdfd3>
- Hachisu, I., Kato, M., Kato, T., & Matsumoto, K. 2000, *ApJL*, 528, L97, <https://doi.org/10.1086/312684>
- Hachisu, I., Kato, M., & Matsumoto, K. 2024, *ApJ*, 965, 49, <https://doi.org/10.3847/1538-4357/ad2a45>
- Hachisu, I., Saio, H., Kato, M., Henze, M., & Shafter, A. W. 2020, *ApJ*, 902, 91,
<https://doi.org/10.3847/1538-4357/abb5fa>
- Hounsell, R., Bode, M. F., Hick, P. P., et al. 2010, *ApJ*, 724, 480, <https://doi.org/10.1088/0004-637X/724/1/480>
- Hung, L. W., Chen, W. P., & Walter, F. M. 2012, 9th Pacific Rim Conference on Stellar Astrophysics. Proceedings of a conference held at Lijiang, China in 14-20 April 2011. ASP Conference Series, Vol. 451. Edited by S. Qain, K. Leung, L. Zhu, and S. Kwok. San Francisco: Astronomical Society of the Pacific, 2011., p.271
- Imamura, K., & Tanabe, K. 2012, *PASJ*, 64, 120,
<https://doi.org/10.1093/pasj/64.6.120>
- Jurdana-Šepić, R., Ribeiro, V. A. R. M., Darnley, M. J., Munari, U., & Bode, M. F. 2012, *A&A*, 537, A34
<https://doi.org/10.1051/0004-6361/201117806>
- Kato, M., & Hachisu, I., 1994, *ApJ*, 437, 802,
<https://doi.org/10.1086/175041>
- Kato, M., Saio, H., Hachisu, I., & Nomoto, K. 2014, *ApJ*, 793, 136, <https://doi.org/10.1088/0004-637X/793/2/136>
- Kato, M., Saio, H., & Hachisu, I. 2022a, *PASJ*, 74, 1005,
<https://doi.org/10.1093/pasj/psac051>
- Kato, M., Saio, H., & Hachisu, I. 2022b, *ApJL*, 935, L15,
<https://doi.org/10.3847/2041-8213/ac85c1>
- Kato, M., Saio, H., & Hachisu, I. 2022c, *RNAAS*, 6, 258,
<https://doi.org/10.3847/2515-5172/aca8af>
- Kato, M., Saio, H., & Hachisu, I. 2024, *PASJ*, 76, 666,
<https://doi.org/10.1093/pasj/psae038>
- König, O., Wilms, J., Arcodia, R., et al. 2022, *Nature*, 605, 248, <https://doi.org/10.1038/s41586-022-04635-y>
- Lockwood, G. W., & Millis, R. L. 1976, *PASP*, 88, 235,
<https://doi.org/10.1086/129935>
- Maehara, H., Arai, A., & Isogai, M. 2009, *CBET*, 2055, 2
- Maehara, H., & Imamura, K. 2009, *CBET*, 2055, 3

- Mason, E., Ederoclite, A., Williams, R. E., Della Valle, M., Setiawan, J. 2012, *A&A*, 544, A149, <https://doi.org/10.1051/0004-6361/201219556>
- Mason, E., & Munari, U. 2014, *A&A*, 569, A84, <https://doi.org/10.1051/0004-6361/201424274>
- McLaughlin, D. B. 1942, *ApJ*, 95, 428, <https://doi.org/10.1086/144414>
- Munari, U., Dallaporta, S., Castellani, F., et al. 2013a, *MNRAS*, 435, 771, <https://doi.org/10.1093/mnras/stt1340>
- Munari, U., Henden, A., Dallaporta, S., & Cherini, G. 2013c, *IBVS*, 6080, 1
- Munari, U., Maitan, A., Moretti, S., Tomaselli, S. 2015, *NewA*, 40, 28, <https://doi.org/10.1016/j.newast.2015.03.008>
- Munari, U., Mason, E., & Valisa, P. 2014, *A&A*, 564, A76, <https://doi.org/10.1051/0004-6361/201323180>
- Munari, U., Ribeiro, V. A. R. M., Bode, M. F., & Saguner, T. 2011, *MNRAS*, 410, 525, <https://doi.org/10.1111/j.1365-2966.2010.17462.x>
- Munari, U., Valisa, P., Milani, A., & Cetrulo, G. 2013b, *ATel*, 5297, 1
- Munari, U., & Zwitter, T. 1997, *A&A*, 318, 269
- Muraoka, K., Kojiguchi, N., Ito, J., et al. 2024, *PASJ*, 76, 293, <https://doi.org/10.1093/pasj/psae010>
- Ness, J.-U., Drake, J. J., Starrfield, S., et al. 2011, *ATel*, 2418, 1
- O'Brien, T. J., Muxlow, T. W. B., Stevens, J., et al. 2010, *ATel*, 2434, 1
- Ootsuki, I., Ohshima, O., Watanabe, O., et al. 2009, *IAUC*, 9098, 2
- Page, K. L., Osborne, J. P., Kuin, N. P. M., et al. 2013, *ATel*, 5470, 1
- Page, K. L., & Beardmore, A. P. 2013, *ATel*, 5429, 1
- Page, K. L., Kuin, N. P., Osborne, J. P., et al. 2014, *ATel*, 5967, 1
- Payne-Gaposchkin, C. 1957, *The galactic Novae* (Amsterdam: North-Holland)
- Pei, S., Orio, M., Ness, J.-U., & Ospin, N. 2021, *MNRAS*, 507, 2073, <https://doi.org/10.1093/mnras/stab2298>
- Ragan, E., Brozek, T., Suchomska, K., et al. 2009, *ATel*, 2327, 1
- Raj, A., Banerjee, D. P. K., & Ashok, N. M. 2013, *MNRAS*, 433, 2657, <https://doi.org/10.1093/mnras/stt946>
- Ribeiro, V. A. R. M., Bode, M. F., Darnley, M. J., et al. 2013, *MNRAS*, 433, 1991, <https://doi.org/10.1093/mnras/stt856>
- Rieke, G. H., & Lebofsky, M. J. 1985, *ApJ*, 288, 618, <https://doi.org/10.1086/162827>
- Rudy, R. J., Prater, T. R., Russell, R. W., Puetter, R. C., & Perry, R. B. 2009, *CBET*, 2055, 1
- Ruggles, C. L. N., & Bath, G. T. 1979, *A&A*, 80, 97
- Schaefer, B. E. 2018, *MNRAS*, 481, 3033, <https://doi.org/10.1093/mnras/sty2388>
- Schaefer, B.E., 2022a, *MNRAS*, 517, 3640, <https://doi.org/10.1093/mnras/stac2089>
- Schaefer, B. E. 2022b, *MNRAS*, 517, 6150, <https://doi.org/10.1093/mnras/stac2900>
- Schaefer, G. H., Walter, F. M., Hounsell, R., Hillman, Y. 2022, *MNRAS*, 517, 3864, <https://doi.org/10.1093/mnras/stac2923>
- Schandl, S., Meyer-Hofmeister, E., & Meyer, F. 1997, *A&A*, 318, 73
- Schmidtke, P. C., Cowley, A. P., Taylor, V. A., Crampton, D., & Hutchings, J. B. 2000, *ApJ*, 1200, 935, <https://doi.org/10.1086/301482>
- Schwarz, G. J., Ness, J.-U., Osborne, J. P., et al. 2011, *ApJS*, 197, 31, <https://doi.org/10.1088/0067-0049/197/2/31>
- Sekiguchi, K., Feast, M. W., Whitelock, P. A., et al. 1988, *MNRAS*, 234, 281, <https://doi.org/10.1093/mnras/234.2.281>
- Sekiguchi, K., Catchpole, R. M., Fairall, A. P., et al. 1989, *MNRAS*, 236, 611, <https://doi.org/10.1093/mnras/236.3.611>
- Selvelli, P., & Gilmozzi, R. 2019, *A&A*, 622, A186, <https://doi.org/10.1051/0004-6361/201834238>
- Shafter, A., Clark, J. G., & Hornoch, K. 2023, *RNAAS*, 7, 191, <https://doi.org/10.3847/2515-5172/acf5e8>
- Shore, S. N., Mason, E., Schwarz, G. J., et al. 2016, *A&A*, 590, A123, <https://doi.org/10.1051/0004-6361/201527856>
- Sun, B., Orio, M., Dobrotka, A., et al. 2020, *MNRAS*, 499, 3006, <https://doi.org/10.1093/mnras/staa3012>
- Takeda, L., & Diaz, M. 2015, *New Astronomy*, 39, 64, <https://doi.org/10.1016/j.newast.2015.03.005>
- Thoroughgood, T. D., Dhillon, V. S., Littlefair, S. P., Marsh, T. R., & Smith, D. A. 2001, *MNRAS*, 327, 1323, <https://doi.org/10.1046/j.1365-8711.2001.04828.x>
- Walter, F. M., & Battisti, A. 2011, *AAS Meeting*, 217, id.338.11
- Walter, F. M., Battisti, A., Towers, S. E., Bond, H. E., & Stringfellow, G. S. 2012, *PASP*, 124, 1057, <https://doi.org/10.1086/668404>
- Wolf, W. M., Bildsten, L., Brooks, J., et al. 2013, *ApJ*, 777, 136, <https://doi.org/10.1088/0004-637X/777/2/136> (Erratum: 2014, *ApJ*, 782, 117, <https://doi.org/10.1088/0004-637X/782/2/117>)
- Williams, R. 2012, *AJ*, 144, 98, <https://doi.org/10.1088/0004-6256/144/98>

Yamaoka, H., Itagaki, K., Guido, E. 2009, IAUC, 9098, 1